



# A comparison of bulk versus laser ablation trace element analyses in banded iron formations: Insights into the mechanisms leading to compositional variability

Leslie J. Robbins<sup>a,\*,1</sup>, Kurt O. Konhauser<sup>a</sup>, Tyler J. Warchola<sup>a</sup>, Martin Homann<sup>b</sup>, Marie Thoby<sup>b</sup>, Ian Foster<sup>b</sup>, Aleksandra M. Mloszewska<sup>c</sup>, Daniel S. Alessi<sup>a</sup>, Stefan V. Lalonde<sup>b</sup>

<sup>a</sup> Department of Earth & Atmospheric Sciences, University of Alberta, Edmonton, Alberta T6G 2E3, Canada

<sup>b</sup> European Institute for Marine Studies, CNRS-UMR6538 Laboratoire Géosciences Océan, Technopôle Brest-Iroise, 29280 Plouzané, France

<sup>c</sup> Earth Sciences Department, University of Toronto, Toronto, Ontario M5S 3B1, Canada

## ARTICLE INFO

Editor: Michael E. Böttcher

### Keywords:

Banded iron formations  
Hammersley Basin  
Nuvvuagittuq Supracrustal Belt  
Laser ablation  
Bulk digestions  
Trace elements

## ABSTRACT

Banded iron formations (BIF) represent one of the few chemical sedimentary archives available for exploring the redox state of the Precambrian atmosphere-ocean system and the marine availability of biologically critical trace nutrients through time. Temporal records compiled for a number of trace elements show a relatively wide spread in concentrations spanning several orders of magnitude within a single deposit. It has been suggested that this spread is present in both bulk rock digestion and laser ablation data, however, the comparability of data from the two methods has not been thoroughly evaluated. Here, we provide a statistical assessment of how comparable laser ablation data of individual BIF hematite and magnetite grains are to one another, as well as how closely averages of laser ablation data approximate bulk rock values. To do so, we use (laser ablation)-high resolution inductively coupled plasma mass spectrometry ((LA)-HR-ICP-MS) data from 14 BIF slabs and corresponding powders that span four different formations. We focus in particular on BIF from the  $\geq 3.75$  Ga Nuvvuagittuq Supracrustal Belt (Québec, Canada) and multiple BIF deposits of the 2.6–2.45 Ga Hammersley Group (North Western Australia), representing deposits separated by over a billion years and of differing metamorphic grade. The scaling between selected transition metals is also evaluated in light of expectations for possible delivery mechanisms of trace elements from seawater to BIF precursor sediments – the adsorption to hydrous ferric oxides, biological vectors, and detrital influence. Our findings show that average trace element concentrations between bulk versus laser ablation data typically vary within an order of magnitude. Furthermore, reproducibility between the two methods appears to be independent of formation age, metamorphic grade, or depositional setting. These findings underscore the overall fidelity of the BIF record at capturing seawater compositional signatures at various scales. We demonstrate that evaluations of ancient seawater chemistry using the BIF record are best served by a combined approach utilizing both bulk rock and laser ablation data, as bulk methods offer the most conservative proxy data for ancient seawater composition but may mask significant enrichments or depletions that are detectable at the grain-scale by laser ablation.

## 1. Introduction

Banded iron formations (BIF) are iron- and silica-rich chemical sediments that precipitated from Archean and Paleoproterozoic seawater. Their mineralogy, comprised of hematite, magnetite, chert, siderite, and a variety of accessory Fe(II/III)-silicates, reflects both the primary precursor phases, such as ferrihydrite and amorphous silica, and the cumulative effects of diagenesis to metamorphism (Bekker et al., 2010,

2014; Konhauser et al., 2017). Although their origins are enigmatic, as BIF deposition lack a true modern analogue in today's oxygenated oceans, these deposits have been demonstrated to be critical archives for early atmosphere and ocean chemistry. Based on the preservation of rare earth element and yttrium (REE + Y) patterns characteristic of seawater, it has been suggested that BIF record trace element enrichments reflective of marine conditions contemporaneous to their deposition (e.g., Bau and Dulski, 1996; Pecoits et al., 2009; Konhauser

\* Corresponding author at: 1-26 Earth Sciences Building, University of Alberta, Edmonton, AB T6G 2E3, Canada.

E-mail address: [lrobbins@ualberta.ca](mailto:lrobbins@ualberta.ca) (L.J. Robbins).

<sup>1</sup> Current address: Department of Geology & Geophysics, Yale University, New Haven, CT 06511, United States of America.

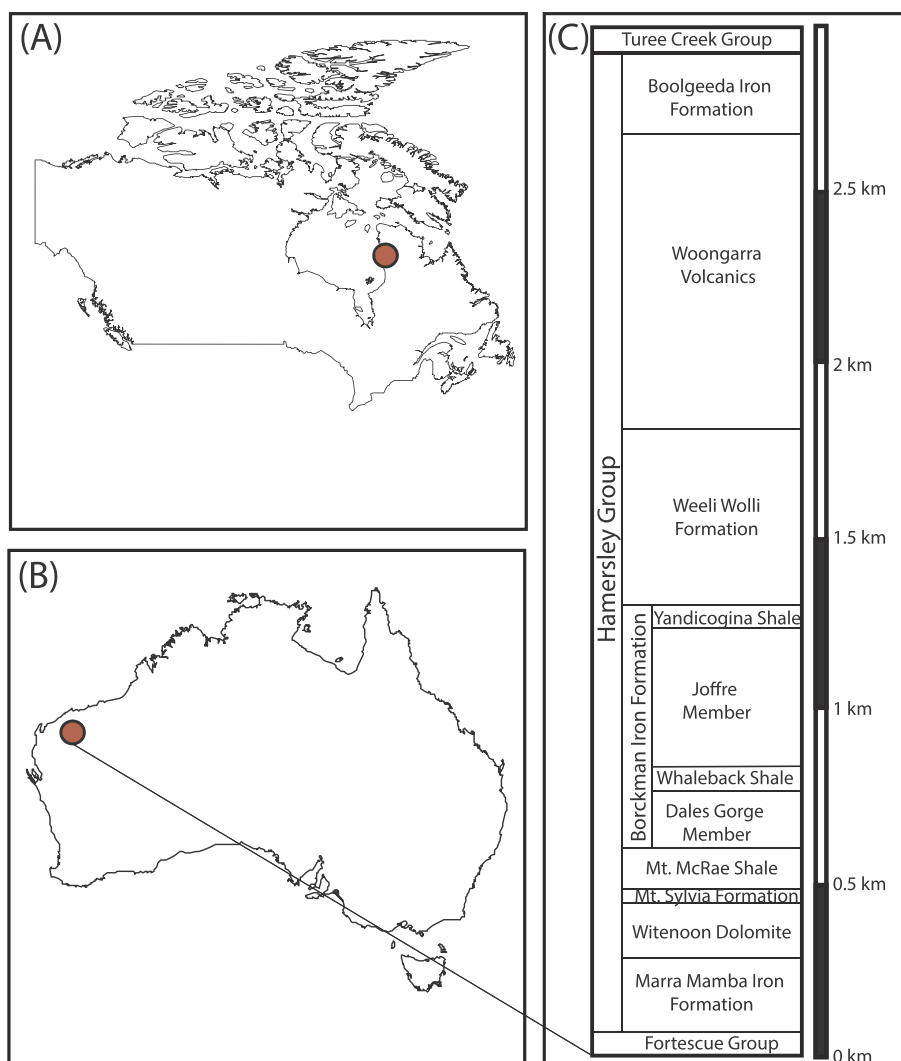
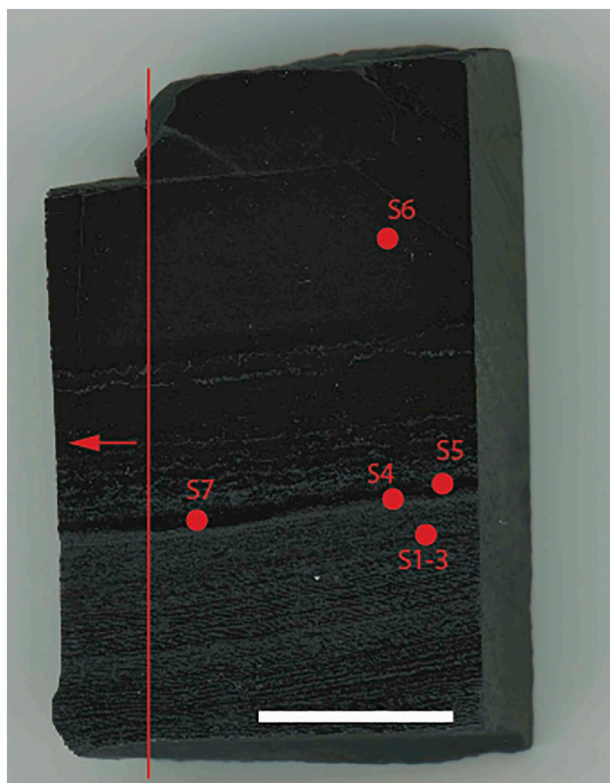


Fig. 1. Schematic diagram showing the locations of (A) the Nuvvuagittuq Supracrustal Belt in northwestern Québec, Canada, and (B) the Hamersley Basin in North Western Australia. (C) The composite stratigraphic column of the Hamersley Group, highlighting the stratigraphic relationship between several of the banded iron formations analyzed here (adapted from Pecoits et al., 2009).

et al., 2009; Mloszewska et al., 2012; Robbins et al., 2013, 2016; Haugaard et al., 2016). BIF have thus been used to track temporal trends in the abundance of biologically critical trace nutrients, including phosphorus (P; Bjerrum and Canfield, 2002; Konhauser et al., 2007; Planavsky et al., 2010a), nickel (Ni; Konhauser et al., 2009, 2015), zinc (Zn; Robbins et al., 2013), cobalt (Co; Swanner et al., 2014), and copper (Cu; Chi Fru et al., 2016). Similarly, redox sensitive trace element abundances in BIF, including chromium (Cr; Konhauser et al., 2011) and uranium (U; Partin et al., 2013a), have provided critical insights on the timing, structure, and tempo of the Great Oxidation Event (GOE), the period in Earth's history 2.45–2.32 Ga when oxygen began to accumulate in the atmosphere (Lyons et al., 2014).

Despite decades of studies on BIF, several aspects regarding their deposition and trace metal enrichment remain cryptic. Foremost amongst these is the variability in trace element concentrations observed within a given deposit or time period, that in some cases spans several orders of magnitude. For instance, in compilations of Ni/Fe ratios (Konhauser et al., 2009, 2015) the spread in BIF values can

exceed two orders of magnitude, especially in samples from before the collapse of the marine Ni reservoir. Similar variability is observed in temporal compilations of Cr, Zn, and Co (Konhauser et al., 2011; Robbins et al., 2013; Swanner et al., 2014, respectively). In the compilation of Zn in BIF through time (Robbins et al., 2013), samples for a given time period can have Zn/Fe ratios that span almost four orders of magnitude in the Paleoproterozoic. This variability is primarily observed in data generated in-situ by laser ablation methods, but it can also be observed in bulk digestions analyzed by solution mode mass spectrometry (e.g., Konhauser et al., 2009, 2015; Robbins et al., 2013). While long-term trends in trace metal abundances are likely a reflection of first-order changes in bulk seawater chemistry, the observed spread in trace element values in BIF has been variously, and informally, proposed to reflect one of several possible explanations that may account for the observed variance in a given BIF deposit or at a certain point in time. These may include: (i) inter- or intra-basinal differences in the availability of transition metals, (ii) the periodic upwelling and subsequent drawdown of transition metals during BIF deposition, (iii)



**Fig. 2.** Example of a BIF slab sampled for bulk digestion HR-ICP-MS and LA-HR-ICP-MS, in this case sample DD98-7 (Joffre Member, Brockman Iron Formation). After polishing, the portion of the sample to the left of the red line was removed, crushed, and powdered for bulk digestion analysis as described in the [Methods](#) section. The sample to the right of the red line was analyzed by LA-HR-ICP-MS. Each spot (1–7) corresponds to three separate laser ablation shots, 44  $\mu\text{m}$  in diameter, into either hematite or magnetite grains. The averaged laser data is then compared to bulk digestion values to determine if a statistical correspondence exists. In some samples, individual laser shots were more widely distributed, but an effort was made to ensure laser shots were distributed throughout the sample. (For interpretation of the references to colour in this figure legend, the reader is referred to the web version of this article.)

the biological drawdown of a transition metal reservoir, (iv) the post-depositional mobilization of trace metals on localized scales, and (v) analytical artifacts resulting from differences in in-situ laser ablation versus bulk analyses. The contribution that different analytical methods have on the observed range in trace element abundances within a given formation has yet to be evaluated in depth. This evaluation is of particular interest as many temporal compilations rely on a combination of bulk digestion analyses and laser ablation generated data from both hematite and magnetite grains. However, the significance of the variability within a given formation, and the statistical compatibility of data generated by laser ablation versus bulk rock digestion, remains a highly under constrained aspect of BIF geochemistry.

Indeed, there have been few studies that have examined the compatibility of laser ablation and solution data with regards to BIF. Previously, [Konhauser et al. \(2009\)](#) have suggested that BIF samples analyzed by laser and bulk methods showed a strong correspondence during the reconstruction of Ni/Fe ratios in BIF through time. [Baldwin et al. \(2011\)](#) used laser ablation analyses to pre-screen chert microbands in order to identify areas to subsample for subsequent digestion

and solution mode analysis, with the aim of identifying chert samples that could be used to reconstruct paleo-marine seawater conditions. Those authors demonstrated that in several instances the laser and solution generated analyses of cherts showed a clear correspondence and as such, laser ablation could provide an effective method for pre-screening samples for subsequent micro-sampling and analysis by total digestion. To this point, however, there has not been a systematic comparison of the comparability of laser ablation data generated by examining the iron oxide mineral phases in BIF, namely hematite and/or magnetite, and bulk values generated through whole sample digestion.

In this study we compare BIF trace element concentration data obtained by bulk digestion and solution-mode analysis versus in-situ laser ablation analysis using HR-ICP-MS data from corresponding pairs of BIF slabs and powders spanning six different formations as well as previously analyzed bulk rock analyses from the same formations. We focus on elemental concentrations and rare earth element ratios, rather than normalized values, as it may be expected that differences in normalizing elemental concentrations (e.g., Fe) should be minor relative (an order of magnitude), suggesting that the trace element concentrations may be the primary source of spread in the BIF record. Samples analyzed include BIF from key examples of Algoma-type and Superior-Type BIF units that vary in depositional setting, age and metamorphic grade. These analyses shed light on the use of bulk versus in-situ methods for investigating paleo-marine signals recorded in BIF and inform our framework for interpreting the range in trace element concentrations observed in large temporal records.

## 2. Banded iron formation samples and localities

Samples examined here were previously collected from two distinct BIF-bearing Precambrian sedimentary sequences: the Eoarchean Nuvvuagittuq Supracrustal Belt in Québec ([Mloszewska et al., 2012](#)), and the Paleoproterozoic Hamersley Basin in Western Australia ([Trendall and Blockley, 1970](#); [Haugaard et al., 2016](#); [Konhauser et al., 2018](#)). The localities and a generalized stratigraphy for the Hamersley Basin are presented in [Fig. 1](#). Also included in the dataset is a single sample from the Eoarchean Isua Formation in Greenland that provides another Eoarchean BIF point for comparison.

### 2.1. Nuvvuagittuq Supracrustal Belt

The Nuvvuagittuq Supracrustal Belt (NSB) is located in north-western Québec, Canada ([Fig. 1A](#)) on the northern shore of Hudson's Bay, and is amongst the oldest crustal rocks preserved. The geological context and composition of the NSB has been reviewed in detail elsewhere (e.g., [O'Neil et al., 2007, 2008, 2011](#); [Mloszewska et al., 2013](#)). Briefly, the belt can be broadly subdivided into three main units: the Ujaraaluk Unit, a cummingtonite-rich amphibolite ([O'Neil et al., 2011](#)), gabbroic and ultramafic conformable bodies ([O'Neil et al., 2007, 2008](#); [Cates and Mojzsis, 2007](#)), and chemical metasedimentary rocks including a 5–30 m thick banded iron formation unit ([Mloszewska et al., 2012, 2013](#)). The NSB underwent extensive retrograde metamorphism from upper amphibolite/lower granulite facies (possibly reaching temperatures up to  $\sim 640^\circ\text{C}$ ) to greenschist facies, and at least three major metamorphic events ([Cates and Mojzsis, 2009](#); [David et al., 2009](#)). Age estimates for the NSB range from  $3751 \pm 10$  Ma ([Cates and Mojzsis, 2007](#)) to  $4280 \pm_{81}^{53}$  based on a  $^{142}\text{Nd}/^{144}\text{Nd}$  vs.  $^{147}\text{Sm}/^{144}\text{Nd}$  isochron age ([O'Neil et al., 2008](#); [O'Neil and Carlson, 2017](#)), placing

**Table 1**  
Isotopes analyzed for the respective element by laser ablation and solution high resolution inductively coupled mass spectrometry ((LA)-HR-ICP-MS).

	Mg	Ca	Ti	V	Cr	Mn	Fe	Co	Ni	Cu	Zn	Sr	Y	La	Ce
LA-HR-ICP-MS	<sup>25</sup> Mg	<sup>43</sup> Ca	<sup>49</sup> Ti	<sup>51</sup> V	<sup>53</sup> Cr	<sup>55</sup> Mn	<sup>58</sup> Fe	<sup>59</sup> Co	<sup>60</sup> Ni	<sup>63</sup> Cu	<sup>66</sup> Zn	<sup>88</sup> Sr	<sup>89</sup> Y	<sup>139</sup> La	<sup>140</sup> Ce
HR-ICP-MS	<sup>25</sup> Mg	<sup>43</sup> Ca	<sup>47</sup> Ti	<sup>51</sup> V	<sup>52</sup> Cr	<sup>55</sup> Mn	<sup>57</sup> Fe	<sup>59</sup> Co	<sup>60</sup> Ni	<sup>65</sup> Cu	<sup>66</sup> Zn	<sup>86</sup> Sr	<sup>89</sup> Y	<sup>139</sup> La	<sup>140</sup> Ce
Resolution in solution mode	High	High	Medium	Medium	Medium	Medium	High	Medium	Medium	Medium	High	Medium	Low	Low	Low
LA-HR-ICP-MS	<sup>141</sup> Pr	<sup>146</sup> Nd	<sup>147</sup> Sm	<sup>151</sup> Eu	<sup>159</sup> Tb	<sup>160</sup> Gd	<sup>161</sup> Dy	<sup>165</sup> Ho	<sup>167</sup> Er	<sup>173</sup> Yb	<sup>175</sup> Lu	<sup>178</sup> Hf	<sup>208</sup> Pb	<sup>232</sup> Th	<sup>238</sup> U
HR-ICP-MS	<sup>141</sup> Pr	<sup>146</sup> Nd	<sup>149</sup> Sm	<sup>151</sup> Eu	<sup>159</sup> Tb	<sup>157</sup> Gd	<sup>165</sup> Dy	<sup>165</sup> Ho	<sup>167</sup> Er	<sup>174</sup> Yb	<sup>175</sup> Lu	<sup>178</sup> Hf	<sup>208</sup> Pb	<sup>232</sup> Th	<sup>238</sup> U
Resolution in solution mode	Low	Medium	Low	Low											

them as some of the oldest crustal rocks preserved, while trace element geochemistry reveals that the chemical sedimentary components likely formed in a marine setting (Mloszewska et al., 2012, 2013). Due to the close association with volcanic units, the BIF of the NSB can be considered Algoma-type. Our interest here lies specifically in the BIF sediments preserved within this Archean terrane. Samples analyzed in this study are the same as previously collected and analyzed by Mloszewska et al. (2012) and are pure chemical sediments, with low detrital input (typically < 1% Al<sub>2</sub>O<sub>3</sub>, < 0.1% TiO<sub>2</sub>, and < 20 ppm high field strength elements).

The BIF samples were taken from an exposed outcrop some 30 m thick, composed of alternating, well-preserved, micro-bands of magnetite, grunerite and locally rich in quartz (for detailed petrography see Mloszewska et al., 2012). The NSB BIF offers a rare glimpse into Eoarchean seawater composition (Mloszewska et al., 2012, 2013), as it is the oldest known BIF that records seawater like signatures. Dodd et al. (2017) reported putative microfossils from the NSB and described them as morphologically similar to iron-oxidizing bacteria. If the biogenicity of these putative fossils can be confirmed, this would make the microfossils of the NSB some of the oldest evidence for life on Earth and underscores the importance of examining the contemporaneous chemical sediments for insights into the depositional paleoenvironment.

## 2.2. Hamersley Group

The Hamersley Basin is located within the Pilbara Craton of Western Australia (Fig. 1B) and hosts the archetype BIF succession. The Hamersley Basin is stratigraphically defined as the Mt. Bruce Supergroup which is comprised of three groups; the Hamersley Group is situated between the underlying Fortescue Group and the overlying Turee Creek Group (Fig. 1C). There are several banded iron formations within the 2.63–2.54 Ga Hamersley Group including the Marra Mamba, Brockman, Weeli Wolli, and Boolgeeda iron formations (Trendall et al., 2004; Fig. 1C). Spatially, the Hamersley Group extends for over 100,000 km<sup>2</sup> and reaches a maximum thickness of up to ~2.5 km with BIF units reaching thicknesses of up to 360 m (Morris, 1993). The Brockman Iron Formation can be further subdivided into the Dales Gorge (2.5–2.45 Ga; Trendall et al., 2004) and Joffre (2.45 Ga; Pickard, 2002) Members, and their deposition corresponds to periods of peak iron precipitation within the Hamersley Basin (Isley, 1995). These BIF were deposited on a large continental platform with minimal detrital input; they are well-banded and are composed almost entirely of chert and iron oxides (Trendall et al., 2004). Banding occurs on a range of scales from millimeter scale microbands to meter scale macrobands (e.g., Trendall and Blockley, 1970). Oxide facies BIF in the Hamersley Basin, including those analyzed here, are typically characterized by magnetite, hematite, chert, as well as accessory phases that include ankerite and iron silicates like riebeckite and stilpnomelane, amongst others (e.g., Pecoits et al., 2009; Haugaard et al., 2016; Warchola et al., 2018). In terms of metamorphic grade, the Hamersley Basin underwent burial metamorphism to prehnite-pumpellyite/lower greenschist facies (Smith et al., 1982). The tectonic setting, stratigraphy, and geochemistry of the Hamersley Group BIF have been previously described in detail (e.g., Trendall and Blockley, 1970; Pecoits et al., 2009; Haugaard et al., 2016).

Samples examined here were collected from cores DD98SPG001 (Krapež et al., 2003) and WW1 (Davy, 1983, 1992), sampling the Joffre and Dales Gorge Members of the Brockman Iron Formation and the Weeli Wolli Iron Formation, respectively. This sample set offers the unique opportunity to examine inter- and intra-formation variability in the trace element composition at the bulk and mineral scales of BIF samples from a single basin.

## 3. Methods

While many of the samples analyzed here have been previously shown to be low in detrital elements and appropriate for paleomarine

reconstructions (e.g., Mloszewska et al., 2012; Konhauser et al., 2018), we do not apply any detrital filters here, as the primary purpose is to assess the similarity of laser ablation and bulk digest generated data.

### 3.1. Sample preparation

BIF slabs selected for laser ablation high resolution inductively coupled plasma mass spectrometry (LA-HR-ICP-MS) were cut and polished at the European Institute of Marine Studies (IUEM), Université Bretagne Occidentale, in Brest, France (Fig. S1). Individual slabs were cut to a size of < 5 cm in length and ~2–4 cm in width to ensure an acceptable fit in the laser ablation cell. Samples for bulk rock analyses were cut from the same BIF slabs, then crushed and powdered (Fig. 2). Bulk digestion samples represent the homogenized mixture of the entire slab. All samples were reduced to < 0.5 cm<sup>3</sup> chips in a tungsten-carbide piston and cylinder using hammer blows. The piston and cylinder were rinsed with water, cleaned with ethanol, and then dried with compressed air between each sample, to ensure no cross-contamination between samples. Afterwards, samples were powdered in a Retsch RS100 vibratory disc mill using an agate grinding set for ~ 7 min. Between BIF samples the entire agate grinding set was cleaned with pure quartz sand for 10 min, then rinsed with water, and cleaned with ethanol.

### 3.2. LA-HR-ICP-MS operating conditions and data treatment

Analyses of BIF samples by LA-HR-ICP-MS analysis at IUEM was

completed in October and November 2016 using a CopexPro 102 Coherent laser attached in-line to a high-resolution Thermo Element2 sector field mass spectrometer, with an additional session in May 2017. The laser was filled with N<sub>2</sub> gas and operated at a wavelength of 193 nm. The laser ablation cell was flushed with helium gas at 200 mL/min. Tuning of the Element2 was optimized based on observed counts for <sup>43</sup>Ca, <sup>138</sup>La, and the Th to U ratio for multiple ablations of the international glass standard NIST612.

Operating conditions included a 44 μm spot size, 10 J, 10 Hz, and an analysis time of approximately 3 min. Each laser ablation data point represents a value obtained by the combined treatment of approximately 50 shots on a single spot in rapid succession at 10 Hz, with the first 10 shots discarded as burn in. Prior to the burn in, the targets were initially ablated with about five shots to clean the surface, and then 30 s was allowed for background levels to fall before initiating the burn in and commencing data acquisition.

During analytical sessions, multiple analyses of international standards were used as calibration points and to constrain methodological error. Measurements of the basaltic glasses BCR-2G and BIR-1G (Table S1), were taken at the start and end of each laser session, where each analytical session lasted approximately 45 min. During longer sampling sessions, additional BCR and BIR spots were analyzed after every ~15 targets. Analyses of BCR-2G were used as calibration points for data treatment while BIR-1G was treated as an unknown to estimate precision (Table S2). All trace element data used for standardization were obtained from GEOREM (<http://georem.mpch-mainz.gwdg.de>) (see Jochum et al., 2005). Laser ablation data were processed using the

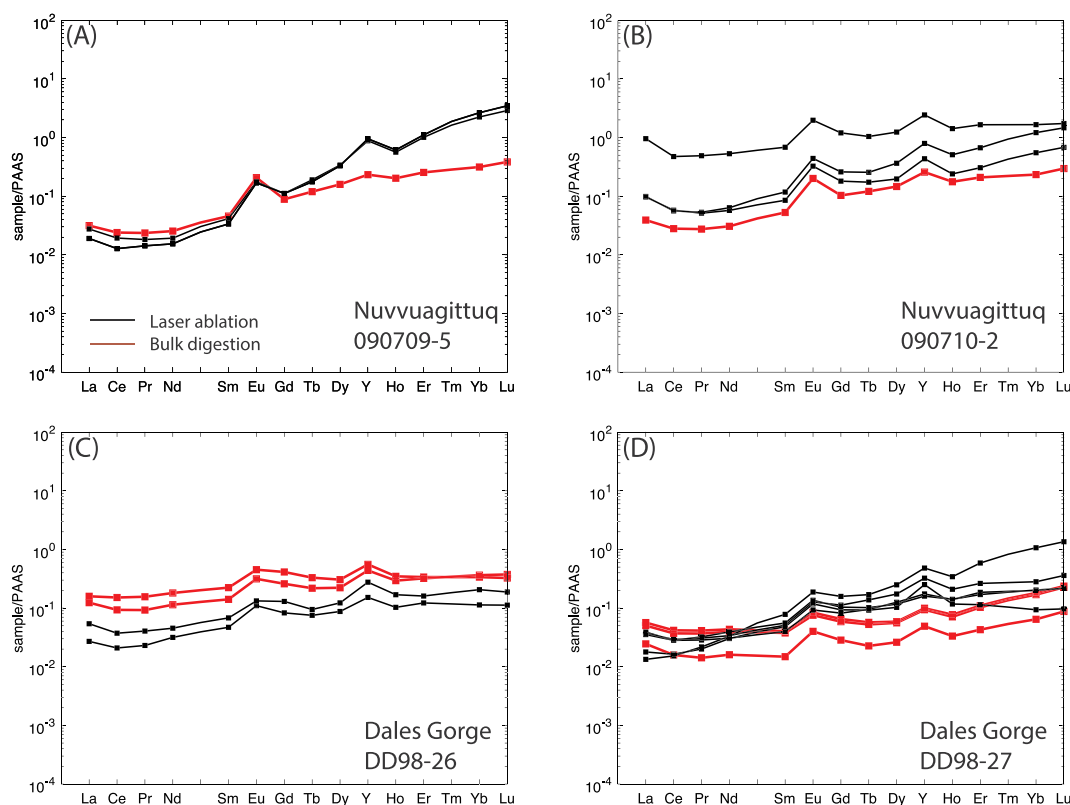


**Fig. 3.** A comparison between REE patterns determined by laser ablation of hematite and magnetite (black symbols and lines) with those determined by bulk digestion (red symbols and lines). Two samples analyzed from the Nuvvuagittuq Supracrustal Belt are shown in A and B (samples 070909-5 and 070910-2, respectively), and the two samples analyzed from the Dales Gorge member of the Brockman iron formation are shown in C and D (samples DD98-26 and DD98-27, respectively). (For interpretation of the references to colour in this figure legend, the reader is referred to the web version of this article.)



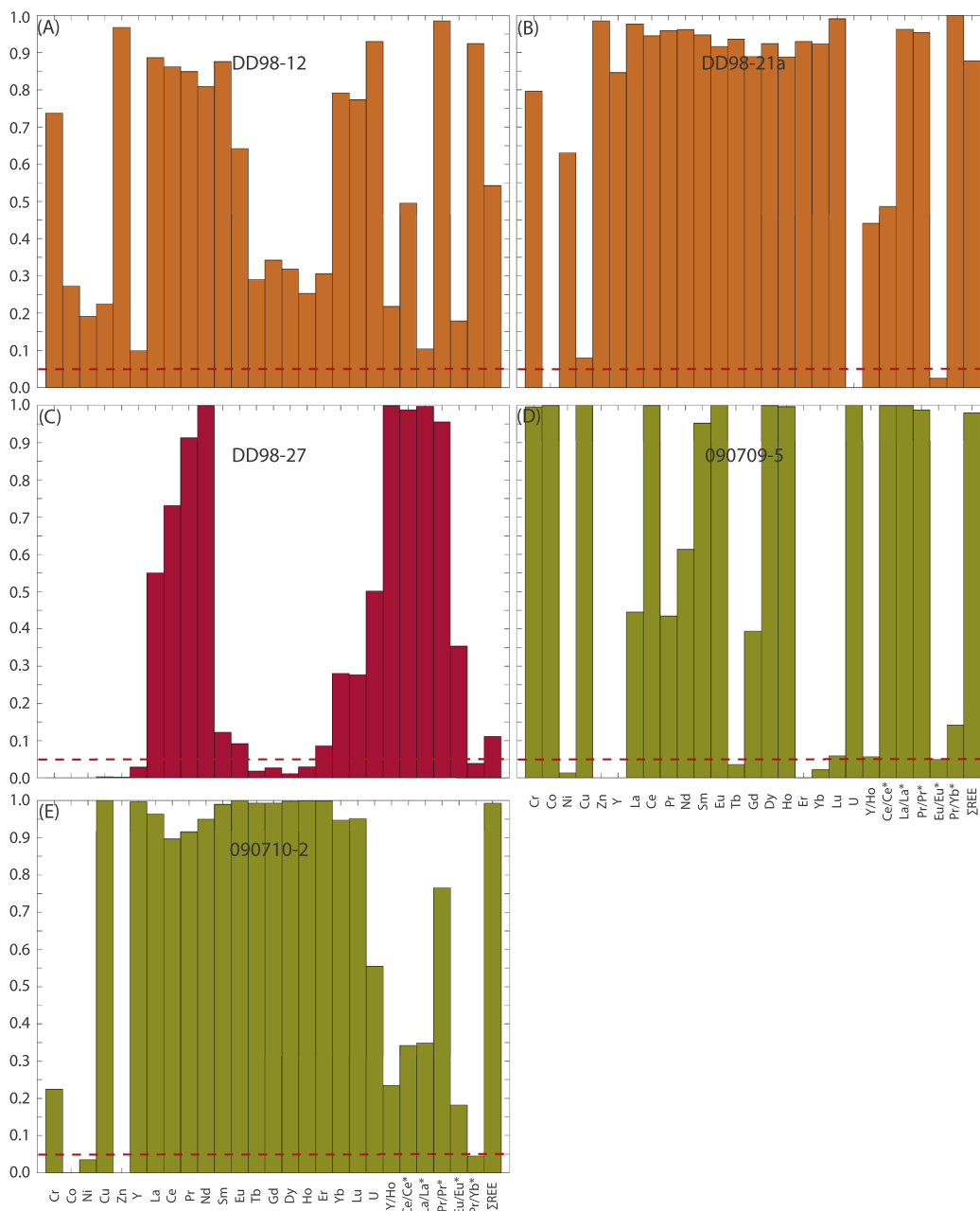


**Fig. 5.** Tukey-Kramer results indicating significant differences between bulk digestion data and magnetite LA-HR-ICP-MS analyses for samples (A) DD98-12 and (B) DD98-21a from the Joffre Member of the Brockman Iron Formation (orange), (C) DD98-27 from the Dales Gorge Member of the Brockman Iron Formation (red), and (D) 090709-5 and (E) 090710-2 from the Nuvvuagittuq Supracrustal Belt (green). A p-value > 0.05, above the red dashed threshold line, indicates that the average values produced by the compared methodologies are not significantly different. (For interpretation of the references to colour in this figure legend, the reader is referred to the web version of this article.)

evaporated overnight at 80 °C to dryness. In the final step, 3 mL of 6 M HCl was added to each residue and samples were heated overnight at 80 °C. Prior to analysis, 100 µL of each sample was evaporated to dryness, re-dissolved in 100 µL concentrated HNO<sub>3</sub> and diluted to 5 mL for a final concentration of 2% HNO<sub>3</sub> for a dilution factor of 1500.

Diluted samples were measured in solution mode on a Thermo

Element2 HR-ICP-MS at IUEM in Brest, France (Table 1). Samples were calibrated by multi-element standards at concentrations of 0.5, 5, and 50 ppb that were measured repeatedly throughout the session. The background concentration of elements in the rinse acids are provided in Table S3. A 5 ppb In (indium) standard was added to each sample, standard, and rinse, and was used to monitor signal stability and correct

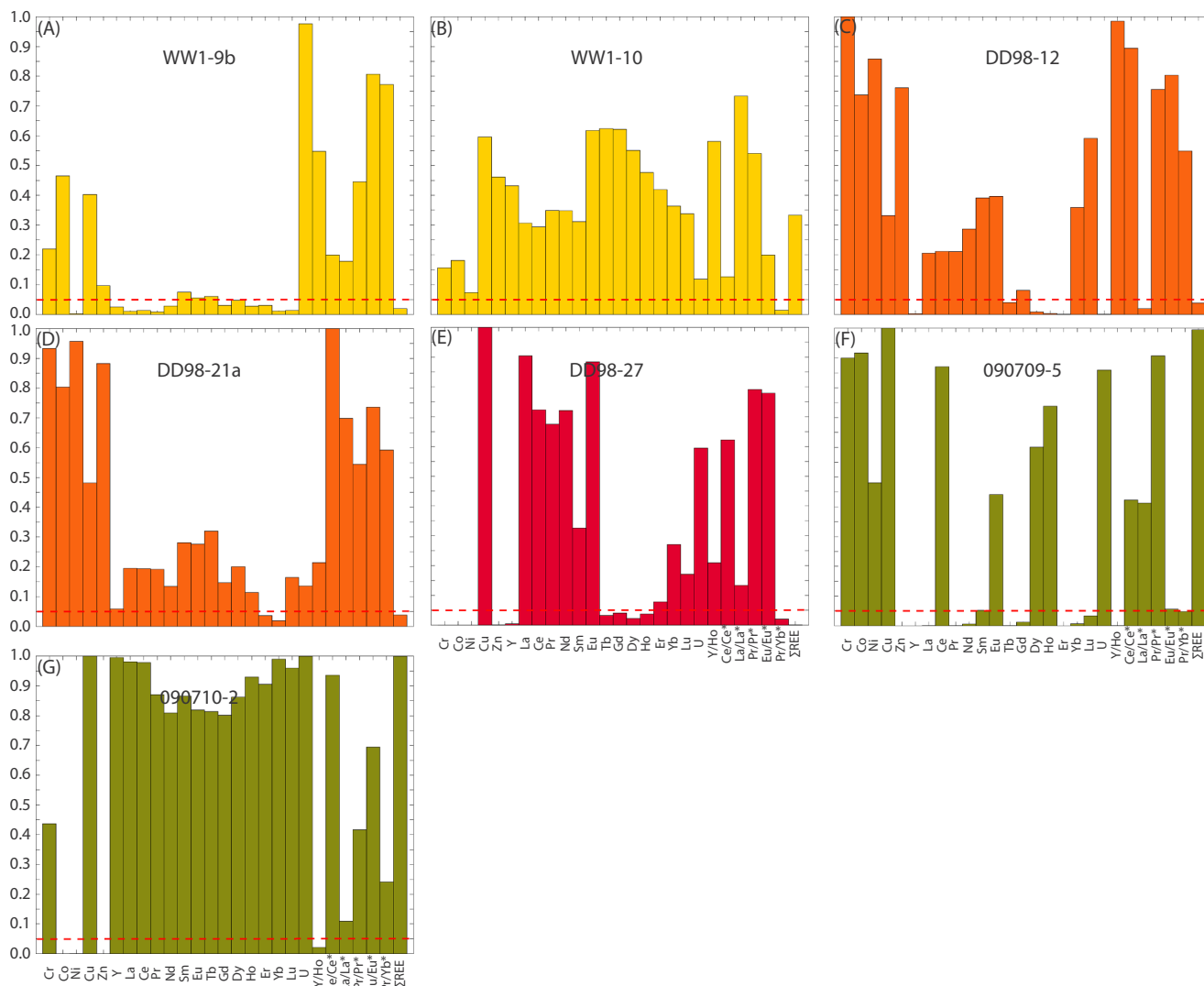


**Fig. 6.** Tukey-Kramer results indicating significant differences between hematite and magnetite LA-HR-ICP-MS analyses for samples (A) WW1-9b and (B) WW1-10 from the Weeli Wollli Iron Formation (yellow), (C) DD98-12 and (D) DD98-21a from the Joffre Member of the Brockman Iron Formation (orange), (E) DD98-27 from the Dales Gorge Member of the Brockman Iron Formation (red), and (F) 090709-5 and (G) 090710-2 from the Nuvvuagittuq Supracrustal Belt (green). A p-value > 0.05, above the red dashed threshold line, indicates that the average values produced by the compared methodologies are not significantly different. (For interpretation of the references to colour in this figure legend, the reader is referred to the web version of this article.)

for instrumental drift across the session. Each sample and standard were bracketed by a rinse for which data was also acquired to determine the method detection limit. Final concentration data were exported and treated in Matlab 2017b to calculate trace element and REE patterns and ratios, using the methods described above.

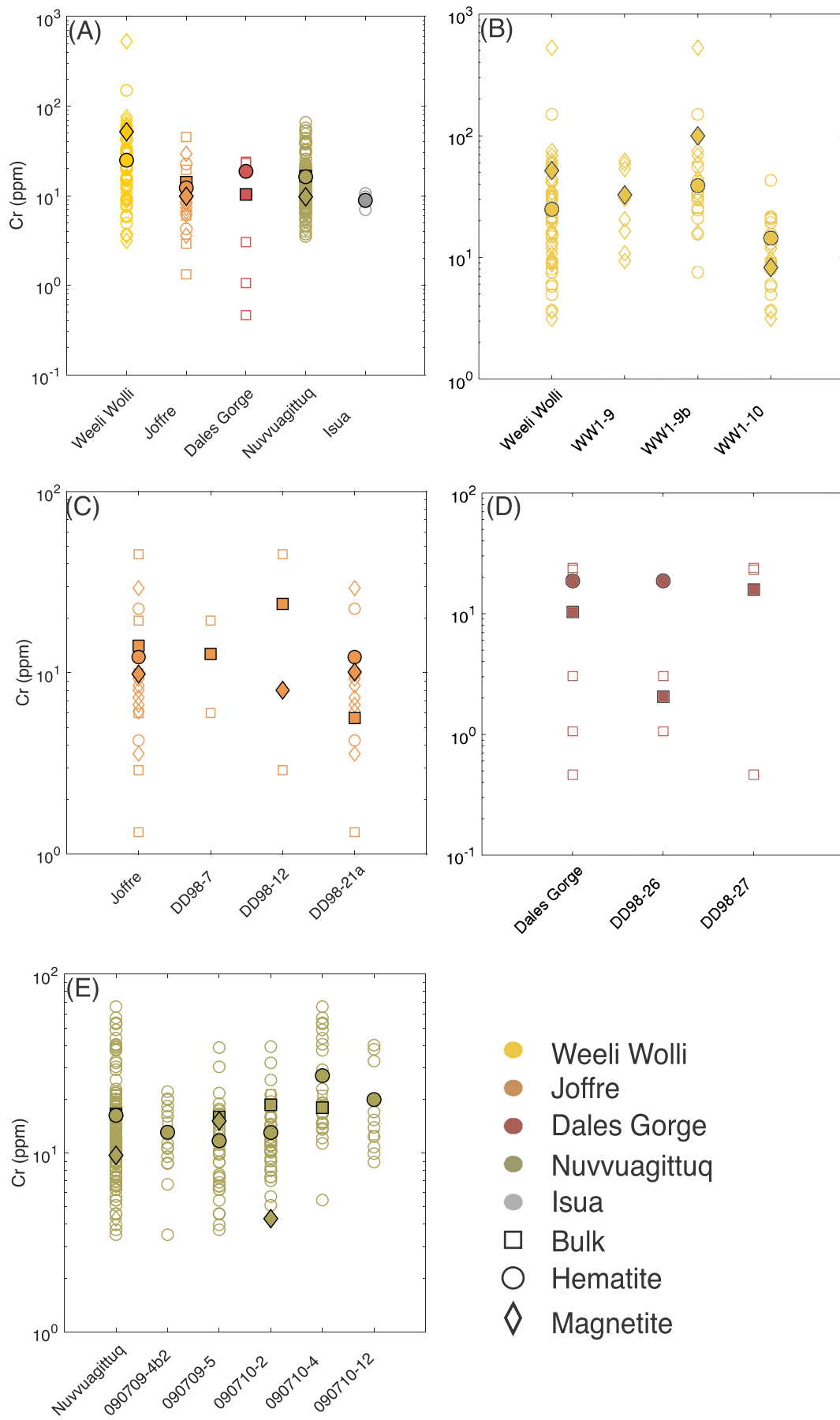
### 3.4. Calculation of rare earth element anomalies

Rare earth element anomalies were primarily calculated after [Bau and Dulski \(1996\)](#), where  $Ce/Ce^*_{PAAS} = Ce_{PAAS} / (0.5La + 0.5Nd)_{PASS}$  and  $Eu/Eu^*_{PAAS} = Eu_{PASS} / (0.67Sm + 0.33Tb)_{PAAS}$ . The Y/Ho ratio was calculated as a simple mass to mass ratio. Due to the influence of La anomalies on Ce/Ce\*, we evaluated the presence of true Ce anomalies using Pr/Pr\*, where positive Pr/Pr\* reveals true negative Ce anomalies,

and negative Pr/Pr\*, true positive Ce anomalies. Pr/Pr\* anomalies were calculated as  $Pr/Pr^*_{PAAS} = Pr_{PAAS} / (0.5Ce + 0.5Nd)_{PASS}$  after [Bau and Dulski \(1996\)](#) and La/La\* anomalies calculated as  $La/La^*_{PAAS} = La_{PAAS} / (3Pr - 2Nd)_{PAAS}$  after [Bolhar et al. \(2004\)](#).

### 3.5. Statistical analysis

To determine whether statistical differences exist between bulk rock solution digests and the laser ablation of hematite and magnetite grains ([Fig. 2](#)), a one-way ANOVA test was performed across a matrix of 20 elements and 7 common ratios or REY indices for each formation. The results of the one-way ANOVA test were then examined by multiple pair-wise comparison of mean values using the Tukey-Kramer method to control for the increasing false positive error rate that accompanies



(caption on next page)

**Fig. 7.** Inter-deposit comparison for chromium (A), and intra-deposit comparisons showing the formation cumulative formation data and that of constituent samples for the Weeli Wolli Iron Formation (B), Joffre Member (C) and Dales Gorge Member (D) of the Brockman Iron Formation, and the BIF of the Nuvvuagittuq Supracrustal Belt (E). Open circles represent hematite LA-HR-ICP-MS data, open diamonds represent magnetite LA-HR-ICP-MS data, and open squares represent bulk digestion data. Filled symbols represent the mean values of the respective methodologies.

an increasing number of pair-wise comparisons (Hsu, 1996; Lalonde et al., 2008). This was performed three times, once for i) bulk rock digests and hematite LA-HR-ICP-MS data, for ii) bulk rock digests and magnetite LA-HR-ICP-MS data, and for iii) hematite and magnetite LA-HR-ICP-MS analyses. In all cases a threshold p-value of  $< 0.05$  indicates that the means of the compared analytical techniques are statistically different. Due to some unavailability of data for the Weeli Wolli Formation samples, the comparison was solely between hematite and magnetite LA-HR-ICP-MS analyses. For samples from the Dales Gorge and Joffre members, as well as the NSB, all three pairwise comparisons were completed whenever hematite, magnetite and bulk data existed for a given sample. If no magnetite data were present for the considered sample, the Tukey-Kramer test considered only differences in bulk versus hematite LA-HR-ICP-MS analysis. For all analyses that returned abundances less than the detection level, for the purpose of statistical tests, these were treated as “NaN” data within Matlab 2017a, or “not a number” whereby samples are indicated to have no valid concentration data for those points. The only sample not subjected to a pairwise comparison was WW1-9, as only magnetite grains were analyzed.

## 4. Results

### 4.1. Limits of detection and precision of analytical methods

The limits of detection for solution analysis and laser ablation are presented in Tables S3 and S4, respectively. The limits of detection are calculated in parts per million for a digestion of 30 mg of powdered BIF. For most elements, detection limits approach the parts per billion range, with the notable exception of some major elements (e.g., Ca, Fe). The treatment of laser data in SILLS returns a detection limit for each element, for each individual shot. As such the maximum, minimum, and average detection limit for each session are summarized in Table S4. Typically, detection limits for transition metals are in the range of 10's of ppm, while for REE + Y detection limits are sub-ppm. As with solution analyses, detection limits for major elements (Mg, Ca, Fe) tend to be higher and are typically in the range of 100–1000 ppm (Table S4).

The duplicate analysis of four samples (DD98-27, 090709-5, 090710-2, and 090710-4) by bulk digestion and HR-ICP-MS returned average percent relative standard deviations (%RSD) of  $< 30\%$  except for Ti (37.18%), Cu (47.32%), La (30.17%), Ce (31.60%), Pr (31.15%), Pb (34.30%), Th (42.25%), and U (48.30%). However, when the %RSD for sample 090710-2 is excluded the average %RSD for solution analyses improves to  $< 10\%$  for all elements except Ti (21.83%), Cr (10.80%), Cu (17.29%), Th (13.78%), and U (20.76%). Repeated analysis of BIR-1G during laser ablation session returned %RSD of  $< 10\%$  for all elements analyzed here except for Ni (16.32%), Th (14.46%) and U (19.01%) based on the individual repeats across all sessions (Table S2). The %RSD based on session averages returns similar but slightly lower relative standard deviations, however, the more conservative %RSD based off individual analyses are presented here. The accuracy for solution mode analyses is better than 20% for all elements except Mg, Mn, Cu, Zn, and Pb which are  $< 25\%$  and Ca and Fe  $< 36\%$  based on a single analysis of the international standard BHVO-2 (Table S1). The estimated accuracy for laser ablation analyses is better than 30% for all

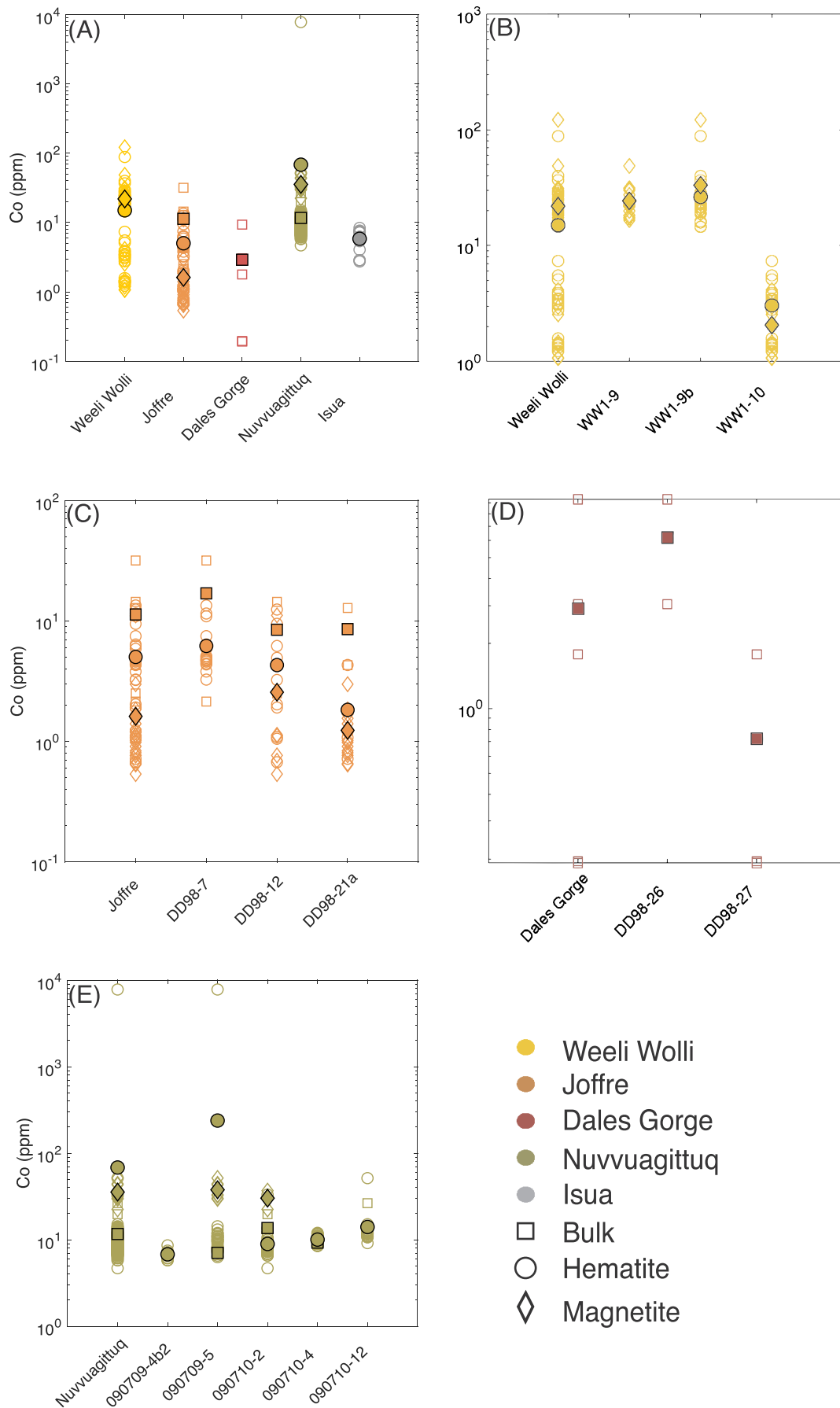
elements except Zn which was closer to 40% based on the repeated analysis of BIR-1G (Tables S1 & S2), although the patterns show a high correspondence with the accepted values (Fig. S2). An assessment of the REE + Y anomalies  $Ce/Ce^*_{PAAS}$  and  $Pr/Pr^*_{PAAS}$  as a function of the counts per second of their constituent elements is provided in Fig. S4; there does not appear to be a systematic control for these anomalies as a function of counts per second of the REE.

### 4.2. Rare earth element patterns

Rare Earth element patterns may host multiple seawater signals, with specific anomalies that may be related to the mixing of water masses, hydrothermalism, and paleoredox. They also permit a rapid visual comparison of results obtained by laser ablation and by bulk digestion. For many shots, full spectra are not available due to some subset of REE being present below the apparent detection limit of that particular shot. This was often the case for samples from the Joffre member of the Brockman iron formation (DD98-7, DD98-12, DD98-21a) and from Isua (the single sample analyzed), while samples from the Dales Gorge member of the Brockman iron formation, from the Weeli Wolli iron formation, and from iron formations in the NSB tended to yield a greater number of full spectra. REE patterns from two samples from the NSB as well as two samples from the Dales Gorge member of the Brockman iron formation are plotted for both laser ablation analyses (black) and analyses after bulk digestion (red) in Fig. 3. In this figure, only laser ablation shots that resolved a complete REE spectrum are presented, however it's important to note that for many shots, some REE are below detection and a complete spectrum is not resolved (see Tables S4–S16), although a sufficient number of REE is often detected to permit the determination of one or more REE anomaly (see Section 3.4 for their description and calculation). The laser spectra represented in Fig. 3 thus represent a selection of shots where the most information was resolved. For these shots, REE concentrations determined by both methods across these samples are remarkably consistent in the  $10^0$ – $10^{-2}$  range (enrichment factor relative to PAAS), with bulk and laser ablation concentration data generally plotting within the same order of magnitude for any given sample and with no systematic offset in concentration evident between the two methods (Fig. 3). Both analytical methods show REE features that are remarkably similar between all samples plotted here, including an enrichment of HREE relative to LREE and the presence of positive La anomalies, positive Eu anomalies, and positive Y/Ho ratios. For all samples analyzed (including samples with incompletely resolved REE spectra), anomalies that were resolved are explored further below as part of the same statistical treatment as other trace element concentrations analyzed in this study.

### 4.3. Bulk solution versus laser generated averages

The LA-HR-ICP-MS results for fifteen BIF slabs from the NSB and Hamersley Group, with paired bulk rock data when available, are summarized in Tables S5–17. Tukey-Kramer tests were performed to examine whether statistical differences exist for three independent sets of pairwise comparisons: (i) bulk digestion versus hematite LA-HR-ICP-MS (Fig. 4), (ii) bulk digestion versus magnetite LA-HR-ICP-MS (Fig. 5),



(caption on next page)

**Fig. 8.** Inter-deposit comparison for cobalt (A), and intra-deposit comparisons showing the formation cumulative formation data and that of constituent samples for the Weeli Wolli Iron Formation (B), Joffre Member (C) and Dales Gorge Member (D) of the Brockman Iron Formation, and the BIF of the Nuvvuagittuq Supracrustal Belt (E).

and (iii) hematite versus magnetite LA-HR-ICP-MS generated data (Fig. 6). In all cases a  $p$ -value  $< 0.05$  indicates that there are significant differences in the mean values generated by the compared methodologies. When data were generated by one method but below detection limits by another (i.e., bulk digestion, but below detection limits for hematite analyzed by LA-HR-ICP-MS), the  $p$ -value was set to 0, indicating a significant difference, as one method generated reliable data but the other failed to do so.

Significant differences between mean values generated by hematite LA-HR-ICP-MS and bulk digestion of BIF samples exist for at least one element in 9 out of 10 samples analyzed here, the lone exception being sample 090710-2 from the NSB (Fig. 3H). When significant differences exist, they tend to be more frequent in the transition metals (e.g., Cr, Cu, Ni, Zn). For several samples (DD98-26, DD9-27), this is the result of several transition metals being below detection limits during LA-HR-ICP-MS (e.g., Co, Ni; Tables S11 & S12). Interestingly, despite many individual REE + Y having  $p > 0.05$ , several of the REE + Y based indices (e.g., Ce/Ce\*<sub>PAAS</sub>, Eu/Eu\*<sub>PAAS</sub>, Pr/Yb) exhibit significant differences when calculated for laser ablation or bulk data, for example in DD98-7 from the Joffre member (Fig. 4A; Table S11).

Similar to the comparison of hematite LA-HR-ICP-MS versus bulk digestion data, magnetite LA-HR-ICP-MS analysis compared to bulk digestion data also has variable instances where significant differences exist between mean values (Fig. 5). While samples from the Joffre Member (Fig. 5A&B) and NSB (Fig. 5E, Table S15) seem to show a strong correspondence overall between mean magnetite and bulk rock data, mean values of samples from the Dales Gorge Member (Fig. 5C; Table S12) and the NSB (Fig. 5D; Table S14) have a higher frequency of elements with significantly different mean values between bulk digestion and magnetite LA-HR-ICP-MS analyses. Part of this may be attributed to low trace element abundances in the magnetite in several of the samples analyzed here (e.g., Co and Ni; Table S12).

The final pairwise comparison considered here, hematite versus magnetite LA-HR-ICP-MS data, also highlights a number of samples where mean concentration values differ significantly (Fig. 6). These differences are especially pronounced in samples from the Weeli Wolli Iron Formation (Fig. 6A, Table S6) and NSB (Fig. 6F; Table S14), while are less significant for other samples from the Weeli Wolli Iron Formation (Fig. 6B; Table S7), and the Joffre Member (Fig. 6C&D; Tables S9 & S10). Some of the significant differences, however, can again be attributed to values in the magnetite or hematite being below detection limits (e.g., Fig. 6E; Table S12).

Overall, it appears that variability in the correspondence of values between compared methodologies is largely dependent on the frequency in which LA-HR-ICP-MS analyses fall below detection limits (e.g., Figs. 4D–E, 5C, & 6E; Tables S11 & S12). Significant differences, however, vary across the samples and within adjacent samples within a given formation (i.e., WW1-9b versus WW1-10, Fig. 6A&B; Tables S6 & S7).

#### 4.4. Inter-deposit variability

Temporal trends in transition metals, including Cr, Co, Ni, Cu, Zn and the redox sensitive element U, are presented in Figs. 7–12, respectively. For Cr (Fig. 7A), mean solution values are relatively

consistent with the baseline provided by the lone sample from the Isua Formation through the NSB, Dales Gorge and Joffre samples. However, the NSB show elevated Cr values based on hematite analyses. The largest spread, spanning almost three orders of magnitude, is present in the Weeli Wolli LA-HR-ICP-MS data, which also has the highest mean Cr concentrations in hematite and magnetite. The Joffre Member and NSB samples show similar mean Cr values in terms of laser and bulk digestion data, and span approximately two orders of magnitude.

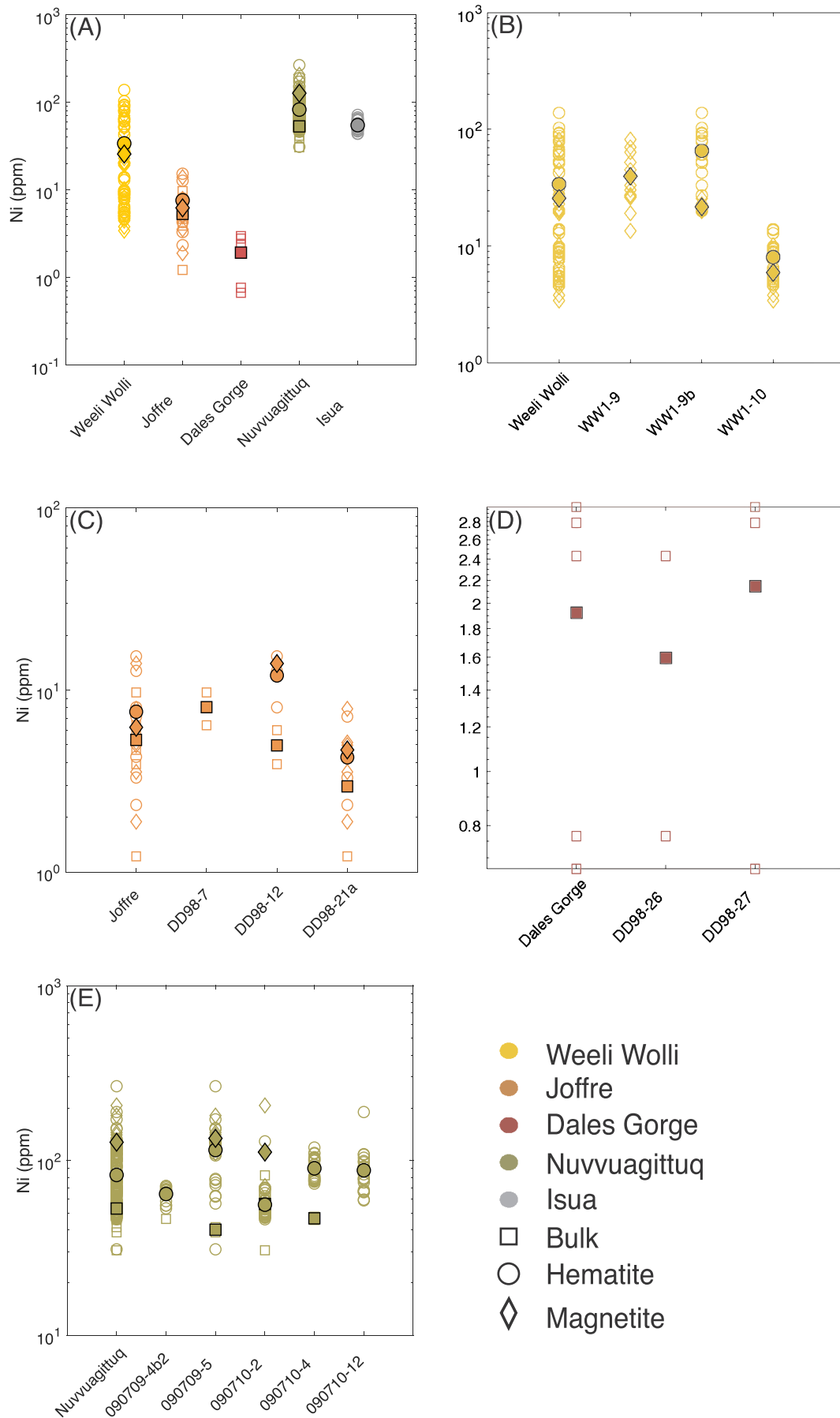
Cobalt (Fig. 8A) shows a wide range in values in the NSB, Joffre Member and Weeli Wolli Iron Formation samples. While the greatest spread is observed in samples from the Weeli Wolli Iron Formation, mean solution values decrease from the NSB to the Dales Gorge Member, before steadily increasing through the Joffre Member, to the mean laser values in the Weeli Wolli Iron Formation. For the Joffre Member samples, mean Co values for hematite and magnetite fall below that of bulk digestion, while for the NSB samples, the opposite trend is observed (Fig. 8A).

Mean nickel concentrations vary systematically between deposits (Fig. 9A) with the greatest bulk digestion mean value observed in the NSB samples. Concentrations then decline in the Dales Gorge Member samples. An uptick in mean bulk values is observed in the Joffre Member (Fig. 9A) but remains about an order of magnitude less than observed in the NSB samples. The greatest spread in values is observed in the laser data from the Weeli Wolli Iron Formation samples, and mean values fall below those for hematite and magnetite in the NSB. In the BIF with the greatest spread in Ni between, namely the Weeli Wolli Iron Formation and the NSB, the majority of magnetite analyses fall below hematite, despite similar mean Ni concentrations (Fig. 9A).

Fig. 10A highlights the temporal pattern in Cu between the formations considered here. Mean values for bulk digestion samples are within an order of magnitude of 10 ppm. Samples from the NSB show a significant spread in values, approaching five orders of magnitude, and in almost all formations, mean Cu values from laser ablation are greater than mean Cu values from bulk digestions. Although mean Cu bulk values remain relatively static (Fig. 10A) through time, there seems to be an increase in the mean Cu laser ablation values up-sequence in the Hamersley Group from the Dales Gorge Member to the Joffre Member and Weeli Wolli Iron Formation.

Similar to Cu, the mean bulk digestion values for Zn (Fig. 11A) show approximately an order of magnitude of variance centered around 10 ppm, with samples from the NSB showing the highest mean Zn bulk values. The greatest spreads are once again observed in samples from the NSB and Weeli Wolli iron formations (Fig. 11A). Interestingly, for formations with data for both hematite and magnetite, magnetite grains appear to record a higher mean Zn value over hematite within each formation, although for the Joffre Member and Weeli Wolli Iron Formation, they mean averages for laser are quite close. In the Joffre Member, (Fig. 11A,C) there is strong convergence between mean Zn values for bulk, hematite, and magnetite measurements.

As with both Cu and Zn, U (Fig. 12A) demonstrates bulk digestion mean values for the NSB, Dales Gorge Member, and Joffre Member samples that cluster within an order of magnitude around 0.1 ppm. For the Dales Gorge and Joffre samples, laser ablation U data corresponds well with the bulk digestion data, especially for hematite. The greatest spread, spanning nearly four orders of magnitude, is observed in the



(caption on next page)

**Fig. 9.** Inter-deposit comparison for nickel (A), and intra-deposit comparisons showing the formation cumulative formation data and that of constituent samples for the Weeli Wolli Iron Formation (B), Joffre Member (C) and Dales Gorge Member (D) of the Brockman Iron Formation, and the BIF of the Nuvvuagittuq Supracrustal Belt (E).

Weeli Wolli Iron Formation. In almost every formation, laser ablation U concentrations are either equal to or below mean bulk digestion values, except for hematite in the NSB (Fig. 12).

Figs. 13–15 highlight several common REE + Y indices for examining paleomarine seawater conditions. Mean Y/Ho ratios, on a gram-per-gram (g/g) basis, dominantly show superchondritic values ( $Y/Ho > 28$ ), a classic indication of seawater-like signatures being preserved. Cerium anomalies (plotted here as  $Pr/Pr^*_{PAAS}$ ) for each of the formations are presented in Fig. 14. Generally, mean values for the Pr anomaly cluster close to 0.95–1.05, but elevated values ( $> 1.05$  and indicating a negative Ce/Ce\* anomaly) are apparent in laser ablation data, suggesting that an oxidative signal may be recorded at the grain scale but diluted or obscured by bulk digestion techniques. The laser ablation data also produces some extreme positive Ce/Ce\* anomalies (indicated by a  $Pr/Pr^*_{PAAS} < 0.95$ ), notably in samples from the Weeli Wolli Iron Formation, that are discussed below in terms of intra-deposit variability. Finally,  $Eu/Eu^*_{PAAS}$  anomalies are presented in Fig. 15. A clear decreasing trend from the baseline Isua Formation sample through to the Weeli Wolli is evident in both the bulk and laser ablation data (Fig. 15A).

#### 4.5. Intra-deposit variability

Figs. 7–12 additionally highlight the intra-deposit variability in trace element abundances by directly comparing the averages of constituent samples alongside the larger formation compilations. Similarly, Figs. 13–15 highlight the intra-deposit variability with respect to the REE + Y ratios discussed above. In this manner the consistency in concentrations between multiple samples from a single formation can be evaluated. Furthermore, instances where a single sample demonstrates an elevated or depleted value and affects the formation average can be highlighted (e.g., Co in hematite grains from sample 090709-5, Fig. 8E; Table S14).

##### 4.5.1. Weeli Wolli Iron Formation

Trace element concentrations in hematite from WW1-9b (Table S6) tend to drive the formation average for individual elements quite high (Figs. 7B–12B), highlighting the ability for a single sample where trace elements may be elevated to skew mean formation values. With the exception of U (Fig. 12B), hematite in WW1-9b is more enriched in trace elements than WW1–10. Despite some low concentrations in magnetite from WW1-10 (e.g., Cr; Fig. 7B; Table S7), formation means are driven by the elevated concentrations in WW1-9 and WW1-9b (Fig. 7B). Similarly, WW1-10 shows a single magnetite with a depressed Y/Ho ratio (Fig. 13B; Table S7), while WW1-9 shows the lowest values with respect to  $Pr/Pr^*_{PAAS}$  and  $Eu/Eu^*_{PAAS}$ . Despite the observed spread in Y/Ho, Ce/Ce\*<sub>PAAS</sub>, and  $Eu/Eu^*_{PAAS}$  (Figs. 13B–15B) mean values in all Weeli Wolli Iron Formation samples analyzed here are markedly similar.

##### 4.5.2. Joffre Member, Brockman Iron Formation

With respect to several indicators examined here, including Cr, Ni, Zn and Y/Ho (Figs. 7C, 9C, 11C, & 13C, respectively), the different datasets from the Joffre Member show some of the most consistent mean values within the formation's larger sample set. For instance, bulk

rock and laser-based mean values cluster relatively tightly for Ni (Fig. 9 C) and U (Fig. 11C). Uranium shows the most intra-formation variability, with a greater spread in sample DD98-21a (Table S10) that approaches three orders of magnitude. While Y/Ho ratios (Fig. 13C) are quite consistent across all samples, in both bulk and laser ablation data,  $Pr/Pr^*_{PAAS}$  show some interesting differences (Fig. 14C). In terms of  $Pr/Pr^*_{PAAS}$  values, while samples show similar bulk digestion mean values, it is evident that a number of laser ablation values are significantly higher than bulk values, reaching up to 1.4 and suggesting that a negative Ce/Ce\* anomaly may be detected in laser but not bulk analyses (Fig. 16). Similarly,  $Eu/Eu^*_{PAAS}$  averages for bulk digestions cluster around 1.9–2.0, while laser generated averages are much lower, clustering around 1.5 (Fig. 15C). Overall, however, the three constituent samples for the Joffre Member show Pr- and Eu-anomalies that are comparable between samples for any given analytical method.

##### 4.5.3. Dales Gorge Member, Brockman Iron Formation

The Dales Gorge Member is represented by two paired powder-slab samples, DD98-26 and DD98-27. Overall, DD98-26 and DD98-27 correspond well in trace element abundances, often within an order of magnitude of one another with respect to both mean bulk digestion and laser ablation values. When present, and above detection limits, magnetite is the more enriched mineral phase (e.g., Cu, Zn, and U; Figs. 10D–12D, Tables S10–11 respectively). Yttrium-holmium ratios (Fig. 13D) have mean bulk digestion and laser ablation values that cluster around 40, with a similar spread, but with lower Y/Ho ratios in DD98-26 and slightly elevated ratios in DD98-27. Both  $Pr/Pr^*_{PAAS}$  and  $Eu/Eu^*_{PAAS}$  exhibit similar behavior in the Dales Gorge Member samples (Figs. 14D & 15D). Interestingly though, it appears that in terms of Y/Ho and  $Pr/Pr^*_{PAAS}$ , hematite grains record lower values in both samples DD98-26 and DD98-27.

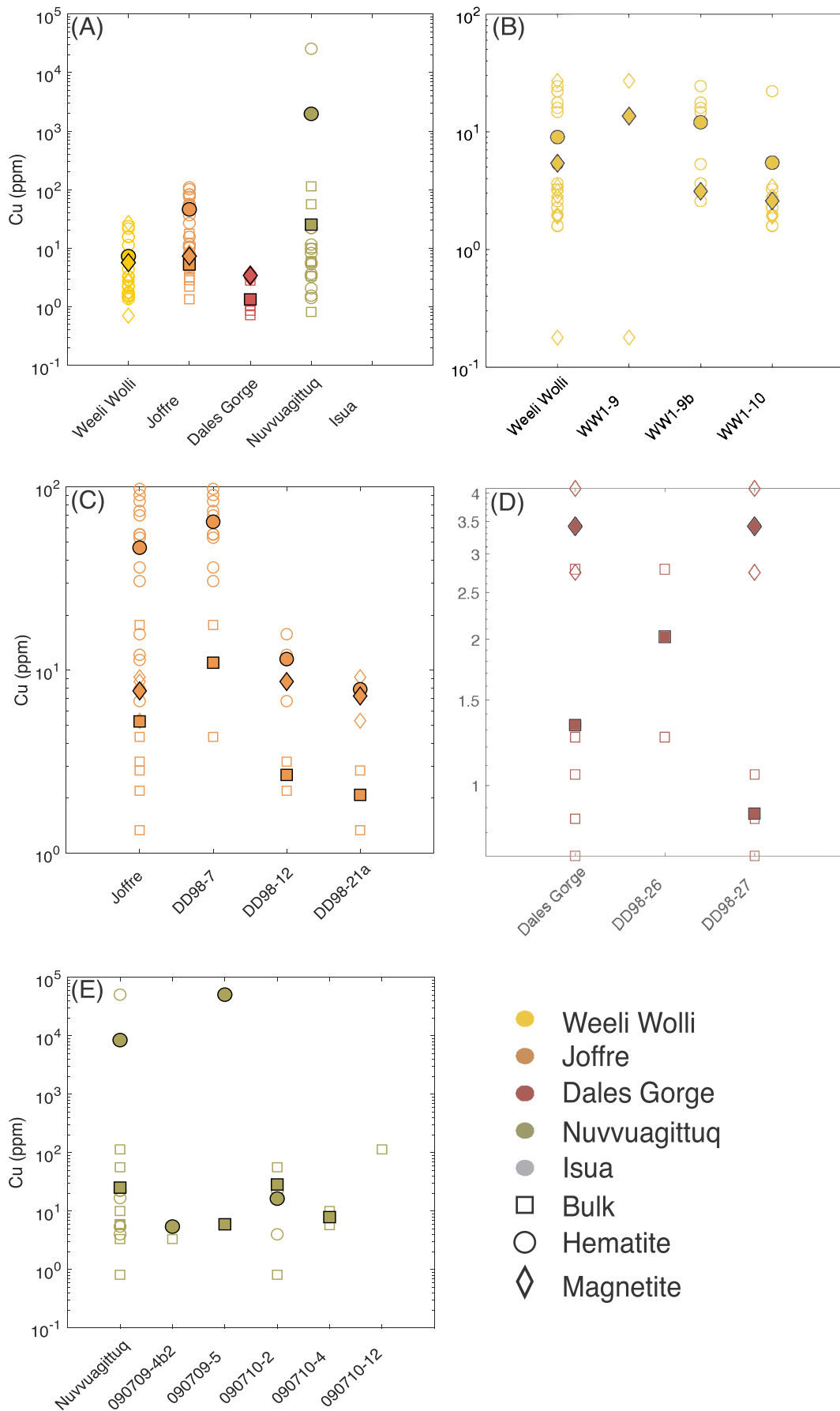
##### 4.5.4. Nuvvuagittuq Supracrustal Belt

The NSB is represented by five samples 090709-4b2, 090709-5, 090710-2, 090710-4, and 090710-12 (Tables S12–16). Magnetite grains were analyzed in both 090709-5 and 090710-2. Magnetite grains in 090710-2 have some of the more extreme trace element abundances (e.g., low Cr and high Zn Figs. 7E, 11E, respectively; Table S15), but Cu is notably absent (Fig. 10E). Most NSB samples generally show a similar level of spread in values.

Similar to Joffre Member samples, the Y/Ho ratios of NSB samples (Fig. 13E) have superchondritic bulk digestion values that are above mean hematite laser ablation values. However, the magnetite mean averages in samples 090709-5 and 090710-2, with regards to Y/Ho ratios, are above that of the bulk digestions. It is remarkable that a number of laser shots produce  $Pr/Pr^*_{PAAS}$  values above 1.05; in all samples, most mean hematite and magnetite values fall close to the mean bulk digestion for  $Pr/Pr^*_{PAAS}$ , with the lowest mean values recorded in magnetites of 090710-2.

#### 4.6. Trace metal systematics

Two distinct methods of examining trace element systematics were considered here: the classic PAAS-normalized cross plot of Ce/Ce\*<sub>PAAS</sub> and  $Pr/Pr^*_{PAAS}$  (Bau and Dulski, 1996; Fig. 16), and the scaling



(caption on next page)

**Fig. 10.** Inter-deposit comparison for copper (A), and intra-deposit comparisons showing the formation cumulative formation data and that of constituent samples for the Weeli Wolli Iron Formation (B), Joffre Member (C) and Dales Gorge Member (D) of the Brockman Iron Formation, and the BIF of the Nuvvuagittuq Supracrustal Belt (E).

between example sets of trace metals (Fig. 17). The sets of trace metals in Fig. 17 were selected to determine what, if any, information could be determined based on the mechanism underlying either BIF deposition, their trace element source or the mechanism of sequestration. In a PAAS-normalized Ce/Ce\*–Pr/Pr\* cross plot, true negative Ce anomalies are distinguished from potential false negative anomalies that might arise in Ce/Ce\* from the positive seawater La anomaly; true negative Ce anomalies will be accompanied by a positive Pr/Pr\* anomaly. It is clear that the majority of bulk samples fall in the field where no true negative Ce anomalies are indicated (Fig. 16). A handful of samples that were analyzed by LA-HR-ICP-MS from the NSB, Joffre, Dales Gorge, and Weeli Wolli iron formations, fall in the lower right-hand field, where true negative Ce- anomalies are indicated. These are discussed in more detail below.

Fig. 17 examines the scaling of two selected pairs of trace elements (1) Cr and Ni, and (2) Ni and Zn. In both cases, these elements show strong linear co-variation. Overlain on the plots are the expected scaling relationships between the elements based on different adsorptive or sequestration mechanisms. Encouragingly, most of the data within these elemental cross plots correspond to a least one of the expected scaling stoichiometries. These correlations and their implications are discussed in Section 5.3.

## 5. Discussion

### 5.1. Statistical reproducibility of bulk versus laser generated trace element concentrations

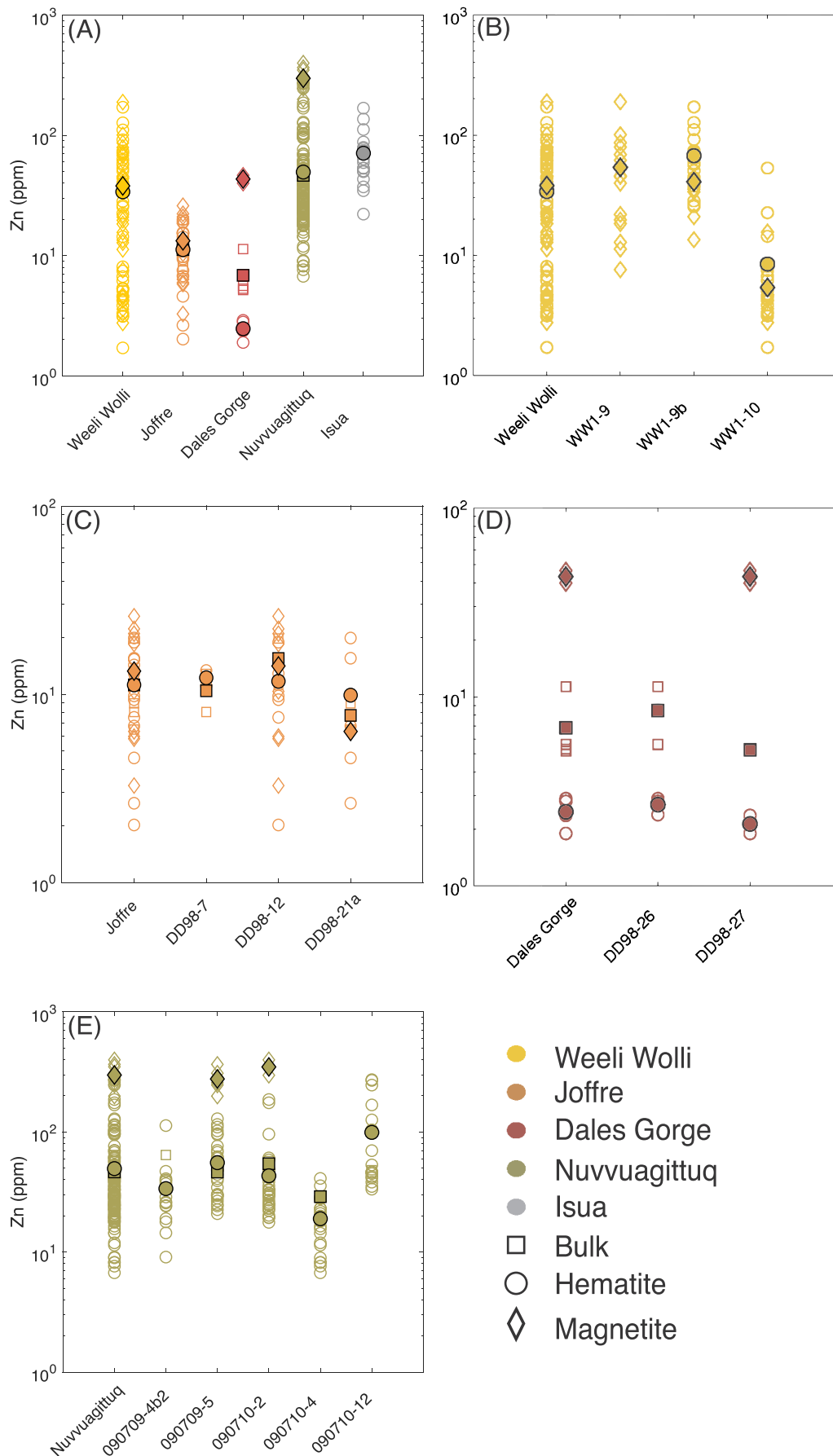
Tukey-Kramer tests (Figs. 4–6) indicate that the reproducibility of bulk digestion trace element geochemistry by LA-HR-ICP-MS analysis of the same sample is a complex and dynamic issue. For some samples, values show good agreement, with p-values dominantly > 0.05 (e.g., Figs. 4C,H,J, 5A, & 6B,D,G). This indicates a strong comparability between the two approaches. Conversely, for a number of samples p-values < 0.05 indicate statistically significant differences between the two methods for a large number of elements (e.g., Figs. 5C,D, 6A,E,&F). Critically, these differences exist in each of the pairwise comparisons considered here: (i) bulk digestion versus laser ablation of hematite grains, (ii) bulk digestion versus laser ablation of magnetite grains, and (iii) laser ablation of hematite versus magnetite grains. Notably, the deposition of BIF from the Hamersley Basin and NSB are separated by over a billion years and underwent different post-depositional alteration histories (See Geological History Sections 2.1 and 2.2). Moreover, BIF from these localities are relatively well-preserved, pure chemical sediments, and do not exhibit signs of significant detrital contamination or post-depositional remobilization (Trendall et al., 2004; Mloszewska et al., 2012; Haugaard et al., 2016). Nevertheless, examples of elements exist within samples from both the Hamersley Group and the NSB for which methodologies dominantly agree ( $p > 0.05$ ; e.g., Figs. 4B,C,H&J, 5 A,B&E, 6B,D&G) or are significantly different ( $p < 0.05$ ; e.g., Figs. 4F&I, 5C, 6A&E). The presence of both agreement and disagreement in samples spanning a vast age range implies that the observed differences are not necessarily a function of age, increasing metamorphism, or depositional setting, as represented by the consideration

of these two disparate BIF deposits. Furthermore, the p-values do not scale with either the ratio of number of laser shots to number of solution analyses or crustal abundance of the elements (data not shown). Some of the difference between methodologies can certainly be ascribed to differences between analytical sessions in instrumental sensitivity and stability during laser ablation. For instance, samples DD98-26 (Fig. 4D; Table S11) and DD98-27 (Figs. 4E, 5C, & 6E; Table S12) were run on days when poor sensitivity during laser ablation sessions resulted in unresolvable concentrations for several transition metals in the majority of laser shots. As a result, a p-value of 0 was assigned to these samples for many of the transition metals, indicating a significant difference as bulk digestions were able to produce transition metal concentrations for these samples.

An interesting observation is that in several instances, while the majority of REE + Y concentrations may be indistinguishable across the pairwise comparisons, some of their respective indices (Y/Ho, Pr/Pr\*<sub>PAAS</sub>, Eu/Eu\*<sub>PAAS</sub>, ΣREE) may vary significantly with p-values falling below the 0.05 threshold (e.g., Figs. 4A, 5B, & 6E). This suggests that when considering elemental ratios and indices, although individual elements may be similar in a pairwise comparison, cumulative differences may drive ratios and indices to statistically different values. Generally, when the pairwise comparisons of REE + Y values returns p-values > 0.05, indices also show a high level of agreement (e.g., Figs. 4C,G,H,&J, 5B, 6A,C&D).

When plotting the laser ablation data and the bulk digestion data simultaneously (Figs. 7–12), bulk digestion mean values typically fall within an order of magnitude of laser mean values, on a formation bases. The laser generated data, however, generally captures a large range in concentrations, an observation that may be attributable to one of several factors. First, the analysis of specific mineral phases, herein hematite and magnetite, generates concentrations in excess of bulk digestion data as concentrations are not subjected to dilution by trace element poor mineral phases, such as chert. Second, within individual samples, variability is frequently observed when hematite or magnetite is the most trace element-enriched phase. For instance, in samples from the Weeli Wolli Formation, magnetite in WW1-9 is typically more trace element rich than in WW1-9b or WW1-10 (Figs. 7–12B), but in WW1-9b and WW1-10, hematite is generally the trace metal rich phase. Similarly, in the Joffre Formation (Figs. 7–12C), mean magnetite values typically fall close to, or below, mean hematite values, and in several instances (e.g., Cr, Co; Figs. 7C & 8C) fall below bulk concentrations as well. Conversely, when concentrations are above detection limits in Dales Gorge Member and NSB samples (Figs. 7–12D&E), magnetite appears to be amongst the more enriched phase in terms of trace element concentrations. This may be the result of diagenetic repartitioning of trace metals on a highly localized scale, which results in mineral specific analyses exceeding the bulk digestion estimates for concentration.

The impact of diagenetic effects on a localized scale may be the underlying cause between disparate mean concentrations between hematite and magnetite grains (e.g., Figs. 7–15). Under such circumstances, trace metals during early diagenesis may be mobilized in localized regions (i.e., on a grain-grain scale or within a BIF microband), then during recrystallization of recalcitrant mineral phases (hematite,



(caption on next page)

**Fig. 11.** Inter-deposit comparison for zinc (A), and intra-deposit comparisons showing the formation cumulative formation data and that of constituent samples for the Weeli Wolli Iron Formation (B), Joffre Member (C) and Dales Gorge Member (D) of the Brockman Iron Formation, and the BIF of the Nuvvuagittuq Supracrustal Belt (E).

magnetite) the mobilized trace metals are sequestered. This would lead to closely spaced LA-HR-ICP-MS analyses of hematite and magnetite within BIF that have significantly different concentrations. This is apparent in many of the samples from the Eoarchean NSB (e.g., Figs. 8E & 11E) and from the Hamersley Basin as well (Figs. 11D, 12C), each of which highlights an instance where *p* values fall below 0.05 for a sample (Fig. 6), indicating significantly different hematite versus magnetite mean values within a single sample.

## 5.2. The origin of variability within the trace metal record

### 5.2.1. An environmental signal

Due to their importance as metalloenzyme reaction centers and cofactors, there has been a great deal of interest in reconstructing the availability of transition metals in the ocean through time (e.g., Anbar and Knoll, 2002; Dupont et al., 2010; Robbins et al., 2016). Some of the transition metals investigated here, including Ni, Zn, Co, and Cu, are critical for a number of prokaryotic and eukaryotic enzymes, and the BIF record has been instrumental in reconstructing their respective marine reservoir size and the evolution of their respective abundances through geological time (e.g., Chi Fru et al., 2016; Konhauser et al., 2009, 2015; Robbins et al., 2013, 2016; Swanner et al., 2014). Previous investigations focused on chemical sedimentary and organic-rich siliclastic records (namely BIF and black shales) have indicated relatively static marine abundances for both Cu and Zn through much of the Archean and Proterozoic (Chi Fru et al., 2016; Robbins et al., 2013; Scott et al., 2013). The deposit comparisons presented here offer only a small sub set of the temporal trends for Cu and Zn (Figs. 10A & 11A). However, similar to the above-mentioned compilations, the spread in values from both laser ablation and bulk digestion techniques are relatively small, with the majority of samples falling within about an order of 10 ppm. This observation lends support to the hypothesis that the concentrations of these transition metals may be buffered by organic ligands (see Robbins et al., 2013), or at least were characterized by relatively long residence times.

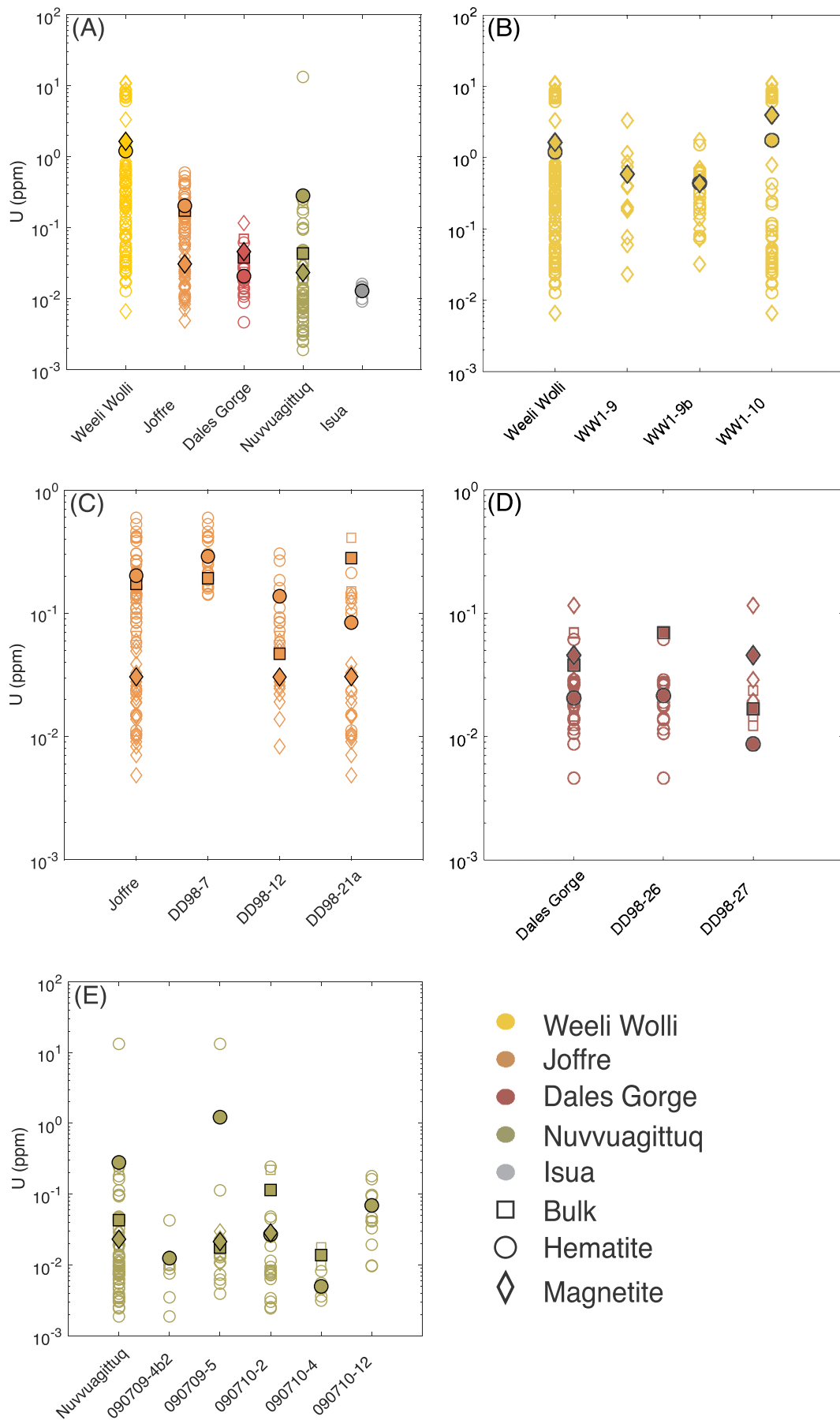
Cobalt (Fig. 8A) and Ni (Fig. 9A) similarly show mean values that fall within about an order of magnitude for each formation. Cobalt appears to be relatively enriched in the  $\geq 3.75$  Ga NSB BIF, dropping in the Dales Gorge and Joffre members, and then increasing as the Weeli Wolli Iron Formation is deposited. The order of magnitude decline in average bulk Ni concentrations observed (Fig. 9A) between BIF samples from the NSB and Hamersley Group is consistent with previous studies on BIF that show a decline in Ni abundances during the Archean; (Konhauser et al., 2009, 2015). Although Weeli Wolli samples show elevated average Ni concentrations in hematite (Fig. 9A&B), these are predominantly due to the elevated concentration observed in WW1-9b and may be the result of localized diagenetic repartitioning or an anomalous input flux of Ni during the deposition of the Weeli Wolli Iron Formation; in either case, it is not representative of the long-term trends recorded by BIF (Konhauser et al., 2009, 2015).

The concentrations of redox sensitive elements (RSE), such as Cr, U, Mo, and V, from BIF and black shales have similarly been used to track the evolution of Earth's surface redox conditions (e.g., Konhauser et al., 2011; Partin et al., 2013a, 2013b; Sahoo et al., 2012; Scott et al., 2008). Two significant increases in RSE are recorded within the sedimentary

record: one coincident with the GOE and a second in the Neoproterozoic at about 850 Ma. While mean formation values remain relatively static across all formations here with respect to RSE and show variance of approximately an order of magnitude around their mean values, maximum values recorded by hematite and magnetite tend to increase as formations become younger (Figs. 7A & 12A). This is especially true for U (Fig. 12A), which likely indicates increasing levels of oxidative weathering in the run-up to the GOE; this signal appears best reflected by maximum values in laser generated data. The increased concentrations of both Cr and U in laser data observed here (Figs. 7A & 12A) is consistent with elevated levels observed in broad compilations for these RSE in BIF immediately before the GOE (Konhauser et al., 2011; Partin et al., 2013a).

Rare earth element signals captured here by both bulk digestion and laser ablation techniques include super chondritic Y/Ho ratios (Fig. 13), variable Ce anomalies (as reflected by  $Pr/Pr^*_{PAAS}$ ; Figs. 14 & 16), and positive Eu-anomalies that decline with decreasing formation age (Fig. 15). Perhaps more interesting though, with respect to the REE, is the presence of negative Ce anomalies revealed by LA-HR-ICP-MS analyses, that are otherwise obscured in bulk digest data (Figs. 14 & 16). While negative Ce anomalies are considered indicative of the presence of oxygen in the water column (e.g., Bau and Dulski, 1996; Bolhar et al., 2004), they are typically absent in BIF predating the GOE (Planavsky et al., 2010b). This observation has previously been used to argue for the prevalence of an anoxic, ferruginous water column during the Archean. However, their absence in BIF predating the GOE may also be attributable to the dilution of  $Ce/Ce^*_{PAAS}$  anomalies that may have occurred in the upper water column through reductive Ce(IV) recycling below a chemocline (c.f., De Carlo and Green, 2002). In our study, the presence of putative negative Ce anomalies identified here by laser ablation in the Eoarchean to Paleoproterozoic BIF (Fig. 16) is at odds with previous data (e.g., Bau and Dulski, 1996; Planavsky et al., 2010b) indicating that negative Ce anomalies indeed exist in formations deposited before the GOE, which, in turn, suggests the presence of oxygen in the early oceans – that is if Ce anomalies are directly tied to the presence of oxygen. Not surprisingly, evidence for an early appearance of oxygenic photosynthesis has grown in recent years, and now includes signs of oxidative cycling of Cr at 3.7 Ga and U at 3.2 Ga, (Frei et al., 2016) and Satkoski et al. (2015), respectively), negatively fractionated Mo isotopes that correlate with Fe/Mn ratios in the 2.95 Ga Sinqeni Formation, Pongola Supergroup (Planavsky et al., 2014), and Fe and S isotope data indicating oxygen production in surface waters of the 2.97 Ga Chobeni Formation, also from the Pongola Supergroup (Eickmann et al., 2018). The negative Ce anomalies identified here by laser ablation (Fig. 16) suggest that the search for early signs of oxygenic photosynthesis may benefit from a small-scale, high spatial resolution approach afforded by in situ analytical techniques such as LA-HR-ICP-MS. Further micro-scale analysis is warranted for formations that have previously shown a lack of negative Ce anomalies in bulk digestions, especially considering the uncertainty associated with differing estimates for the origins of the appearance of oxygenic photosynthesis using genetic approaches (e.g., Shih et al., 2016; Ward et al., 2016; Magnabosco et al., 2018) and those of geochemical indicators (e.g., Planavsky et al., 2014; Satkoski et al., 2015).

The iron in BIF is generally considered to have been sourced from



(caption on next page)

**Fig. 12.** Inter-deposit comparison for uranium (A), and intra-deposit comparisons showing the formation cumulative formation data and that of constituent samples for the Weeli Wolli Iron Formation (B), Joffre Member (C) and Dales Gorge Member (D) of the Brockman Iron Formation, and the BIF of the Nuvvuagittuq Supracrustal Belt (E).

hydrothermal activity, then upwelled onto the shelf where it was ultimately deposited (e.g., Holland, 1973, 1978; Bekker et al., 2014; Konhauser et al., 2017). In this regard, the peak in BIF deposition at ~2.45 Ga (Isley, 1995; Klein, 2005) seemingly coincides with the emplacement of large igneous provinces and enhanced mantle plume activity (e.g., Barley et al., 1997). Since the iron is sourced from hydrothermal processes, the secular decline observed in Eu anomalies preserved in BIF through time (see Fig. 5 in Konhauser et al., 2017) has traditionally been interpreted to represent a waning hydrothermal flux (e.g., Derry and Jacobsen, 1990; Bau and Möller, 1993; Viehmann et al., 2015). While not as stark of a trend as that presented in Konhauser et al. (2017), the Eu-anomalies presented here (Fig. 15) show a progressive decline with increasingly younger formations, reinforcing the idea that high temperature hydrothermal inputs to BIF depositional settings declined progressively into the earliest Paleoproterozoic.

Estimates for BIF depositional rates are uncertain and range in values from a few hundred years to tens of thousands of years per meter of compacted BIF, equating to an accumulation of < 1 mm/year (Morris, 1993; Konhauser et al., 2002; Bekker et al., 2014). When considering consolidation rates on top of these estimates, it is more than likely that a few mm's of BIF represent a depositional period spanning decades, if not hundreds of years. Accordingly, it may be expected that during deposition currents and nutrient fluxes in the depositional basin may well change over such timescales. A recent study by Warchola et al. (2018) highlights this possibility. Through the examination of a high-resolution chemostratigraphic profile of the Boolgeeda Iron Formation, the terminal deposit in the Hamersley Group, the authors identify a pseudo-sinusoidal shift in trace and REE + Y abundances linked to shifting detrital input, attributable to transgressive and regressive events over the course of a signal BIF unit being deposited. As such, some of the variability observed in the trace element concentrations within a BIF deposit are likely a function of localized environmental signals, detectable via high resolution chemostratigraphy but that are masked by the overall first-order trends observed in large temporal compilations (e.g., Konhauser et al., 2009, 2015; Robbins et al., 2013).

Despite a number of instances where bulk and laser data differ significantly for a given sample (Figs. 4–6), it is encouraging that the patterns observed in our sample set coincide well with previously identified temporal trends in trace nutrients, RSE, and REE + Y anomalies such as  $\text{Eu}/\text{Eu}^*_{\text{PAAS}}$ . This suggests that while both bulk digestion and laser ablation data are capable of reproducing paleo-marine seawater trends in trace element concentrations, that laser ablation analyses may provide a more detailed picture of the environmental signal capture within a single BIF deposit.

### 5.2.2. Trace element removal pathways

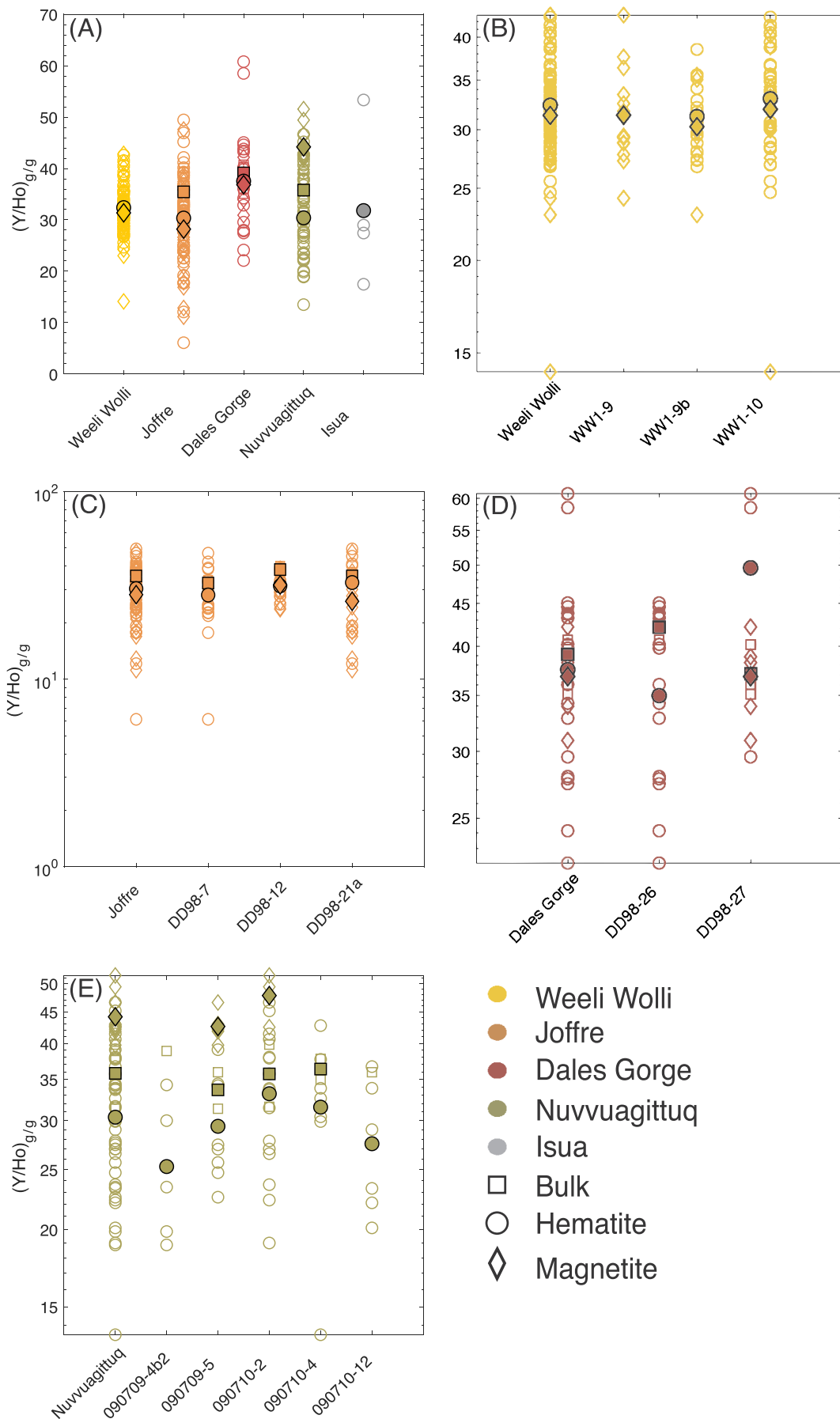
The scaling between selected transition metals was examined for the correspondence to the expected stoichiometric ratios of proposed exit fluxes for trace elements in BIF (Fig. 17). We did this to assess whether transition metal systematics can shed additional light on the mechanisms underpinning trace element sequestration, the dominant controls on BIF deposition, and how this may lead to variations in trace metal concentrations in BIF. While hematite in BIF is commonly thought to have formed through the dehydration of a ferric oxyhydroxide

precursor deposited by abiogenic or biogenic iron oxidation, magnetite is primarily recognized as a diagenetic phase formed as a by-product of dissimilarity Fe(III) reduction or metamorphic reactions of ferric-iron bearing minerals with organic carbon at temperatures above the threshold for bacterial growth (see Konhauser et al., 2017 for a detailed discussion). Konhauser et al. (2018) argued that the trace element stoichiometry of the Dales Gorge Member closely relates to the cellular stoichiometry of anoxygenic photoferrotrophs and thus indicates a role for these bacteria in BIF deposition. Commonly envisioned exit channels for trace elements to BIF include the contribution of detrital material, the adsorption of trace elements to hydrous ferric oxides (e.g., Dzombak and Morel, 1990; Bjerrum and Canfield, 2002; Konhauser et al., 2009), and the association of trace elements with biomass (Konhauser et al., 2002, 2018; Li et al., 2011; Martinez et al., 2016).

Overlain on cross-plots of transition metals are scaling ratios (Table 2) that can be expected for several possible vectors that may have sequestered trace elements into BIF. These scaling ratios were derived from elemental ratios of upper continental crust (Condie, 1993; Rudnick and Gao, 2014), the relative strength of adsorption constants of trace elements to hydrous ferric oxides (Dzombak and Morel, 1990), ratios present in modern seawater (Bruland et al., 2014), and, where possible, stoichiometric ratios characteristic of biomass of the marine photoferrotroph *Rhodovulum iodolum* (Konhauser et al., 2018). The scaling expected due to adsorption to hydrous ferric oxides is represented by the ratio of the site-1 binding constants of Dzombak and Morel (1990) for the respective trace metals.

Curiously, the expected stoichiometric ratios for these exit pathways (Table 2) seem to correlate well with transition metal scaling preserved within BIF by both bulk digest and laser data (Fig. 17). Laser and bulk solution data both show a near-linear scaling between transition metals essential for biological functions and those that are mobilized by oxidative weathering (Cr vs. Ni, Fig. 17A). Nonetheless, there is a divergence in scaling between Ni and Zn, particularly for samples from the NSB. This divergence suggests the NSB may have received additional input from another source of Ni, as samples deviate from the detrital line (Fig. 17B). A clear correspondence is observable between the transition metals and expected detrital, seawater, and phototroph stoichiometries. It is telling that concentrations of detrital indicators are resolvable and non-negligible even in laser ablation shots of pure mineral grains (e.g., Ti; Tables S5–S7; Fig. S3), and that detrital indicators may correlate with other elements that may have strong important sources (e.g., Cr) as a result of their common origin. We suggest that quite simply, the origin of these elements may always be detrital, even at low abundances and entombed as trace constituents in iron oxide minerals. This may explain why samples tend to fall close to the detrital line for Cr relative to Zn (Fig. 17A). Further, there is also an adherence to scaling predicted by ratios of adsorption constants for hydrous ferric oxides as measured by Dzombak and Morel (1990).

As the majority of stoichiometries for exit fluxes are convergent (Fig. 17A&B) it is unlikely that in most cases the sequestration mechanism can be delineated using the transition metal systematics of two selected trace elements. As such a holistic approach that considers multiple trace metals simultaneously, such as that employed by Konhauser et al. (2018), is required to elucidate further information on BIF depositional mechanisms. However, it is quite interesting that bulk



(caption on next page)

**Fig. 13.** Inter-deposit comparison for Y/Ho ratios (g/g) (A), and intra-deposit comparisons showing the cumulative formation data and that of constituent samples for the Weeli Wollie Iron Formation (B), Joffre Member (C) and Dales Gorge Member (D) of the Brockman Iron Formation, and the BIF of the Nuvvuagittuq Supracrustal Belt (E).

values for the Dales Gorge and Joffre members for Ni relative to Zn approach the anoxygenic photoferrototh line derived from the stoichiometries characteristic of *Rhodovulum iodolum* biomass (Konhauser et al., 2018), as one would expect if anoxygenic phototrophs played a large role in BIF deposition.

### 5.2.3. Diagenesis

Effectively all minerals found in BIF are the result of diagenesis and metamorphism (Klein, 2005; Bekker et al., 2014; Konhauser et al., 2017). Accordingly, a critical aspect of exploiting the BIF record is understanding the fate of trace elements during burial and how the trace element distribution in various mineral phases may be a function of secondary repartitioning. The current mineralogy of BIF, namely hematite, magnetite, chert, siderite, and a variety of accessory Fe(II/III)-silicates, reflects both the primary precursor phases and the cumulative effects of diagenesis to low grade metamorphism (Klein, 2005). It is probable that the hematite forms through the dehydration and thermal maturation of a precursor such as ferrihydrite (e.g., Ahn and Buseck, 1990; Sun et al., 2015), while magnetite and siderite are likely the products of Fe(III) reduction coupled to the oxidation of organic carbon (e.g., Konhauser et al., 2005; Johnson et al., 2008). Consistent with this view, experimental diagenetic incubations of a simple admixture of ferrihydrite and glucose at 170 °C and 1.2 kbar, conditions considered to be representative for recrystallization from ferrihydrite to hematite in the Penge Iron Formation, South Africa (e.g., Miyano and Klein, 1984), have been shown to reproduce a mineralogy characteristic of BIF as observed today (e.g., Posth et al., 2013; Köhler et al., 2013). Recent thermochemical Fe(III) reduction experiments (Halama et al., 2016), however, complicate this view as no magnetite was observed when biomass was incubated with either ferrihydrite, goethite, or hematite at 170 °C and 1.2 kbar. This suggests that more recalcitrant forms of biomass adsorbed to the mineral surface may insulate against mineral transformations, or that short term experiments are insufficient for recreating the diagenetic reactions that produce the characteristic stable mineral phases when a more recalcitrant organic carbon source is provided. What is certain is that the mineralogy of BIF is not a direct reflection of the primary minerals that precipitated from the water column when BIF were being deposited.

BIF of various ages have been shown to retain seawater-like REE + Y patterns despite undergoing a range of metamorphic conditions up to, and including, amphibolite facies metamorphism (Bau, 1993; Bau and Dulski, 1996; Bolhar et al., 2004; Pecoits et al., 2009; Mloszewska et al., 2012; Haugaard et al., 2016), indicating that an authigenic marine signal is retained even after diagenesis and metamorphism. Additionally, experimental incubations of ferrihydrite doped with Zn and Ni designed to capture the transition of precursor hydrous ferric oxides to hematite and more crystalline Fe phases have shown that transition metals may be retained by the resultant mineral phases following BIF diagenesis (Robbins et al., 2015), although the distribution amongst specific mineral phases was not examined. The localized mobilization of trace elements during diagenesis and metamorphism can never be entirely ruled out, and likely occurs at very fine spatial scales. For instance, Alibert (2016) demonstrated that the concentration of REE + Y in certain minerals reflect diagenetic processes in BIF, namely apatite and ankerite, while hematite and magnetite tend to

show REE + Y patterns reflective of porewater adsorption processes. Despite this repartitioning, Alibert (2016) demonstrated that diagenetic to metamorphic minerals – e.g., apatite, hematite, siderite – may retain seawater-like REE + Y patterns but differ with respect to concentration. Recently, Oonk et al. (2017, 2018) employed sequential extractions in order to assess the composition of specific mineral fraction within BIF, with the aim of assessing primary versus diagenetic signals. Oonk et al. (2017) focused on extracting three mineralogical phases (i) carbonate, (ii) oxides – hematite and magnetite, and (iii) Fe-silicates, placing an emphasis on understanding the role of these three phases in Mo, Cr, and U cycling. Similarly, Oonk et al. (2018) utilized a sequential extraction method to examine the phase specific distribution of REE + Y. In both studies, critical phase specific associations were identified. For instance, Oonk et al. (2017) found that U tended to be associated with the Fe-silicate fraction, while Oonk et al. (2018) found the oxide fraction to be the lowest in REE + Y abundances and, therefore, the most susceptible to contamination by detrital material. Furthermore, Oonk et al. (2018) suggested that while bulk rock REE + Y composition appears to track seawater composition, that of the oxide phase must be viewed cautiously as it can take on a mixed REE profile following deposition and diagenetic recycling.

These studies, along with results presented here, suggest that the analysis of either trace element rich or poor mineral phases by LA-HR-ICP-MS will induce a greater spread in concentration within a given BIF sample than would otherwise be observed in bulk digests of the same sample. Accordingly, sequential extractions and high-resolution in-situ analysis in future work may continue to shed further light on the mechanisms underlying BIF deposition and diagenesis.

### 5.3. Implications for the interpretation of environmental signal in BIF

The observed spread in trace element concentrations, and trace element to iron ratios, in temporal records (Konhauser et al., 2009, 2015; Robbins et al., 2013, 2016; Partin et al., 2013a; Swanner et al., 2014) is likely due to a combination of heterogeneity at the mineral and hand-sample scale, as well as temporal changes in the concentration of trace elements in seawater. It is worth noting that there are several instances where trace element concentrations fluctuate relative to stratigraphically adjacent samples, and while this fluctuation may be present, even if slightly attenuated in mean bulk values, it also bears out in the respective hematite and/or magnetite mean values. Examples can be seen in Figs. 9E, 11B, & 12C. In Fig. 9E, the bulk value of sample 090710-2 is slightly elevated over the neighboring samples and coincides with an increase in Ni in magnetite grains within this sample, while the hematite average also differs relative to the adjacent samples. Similarly, a slight increase in Cu concentration in two samples from the Joffre Member (DD98-7 and DD98-12; Fig. 10C) is reflected both in bulk average digest and laser ablation generated data. This also bears out for several samples with respect to U in the Joffre Member and NSB BIF samples (Fig. 12C & E), where changes in bulk mean values are reflected by increases or decreases in mineral specific averages between adjacent samples. This would suggest that the observed range in trace metal concentrations within a given formation may itself be a reflection of subtle, more nuanced chemostratigraphic changes during the deposition of a given formation. Importantly, this may be obscured in

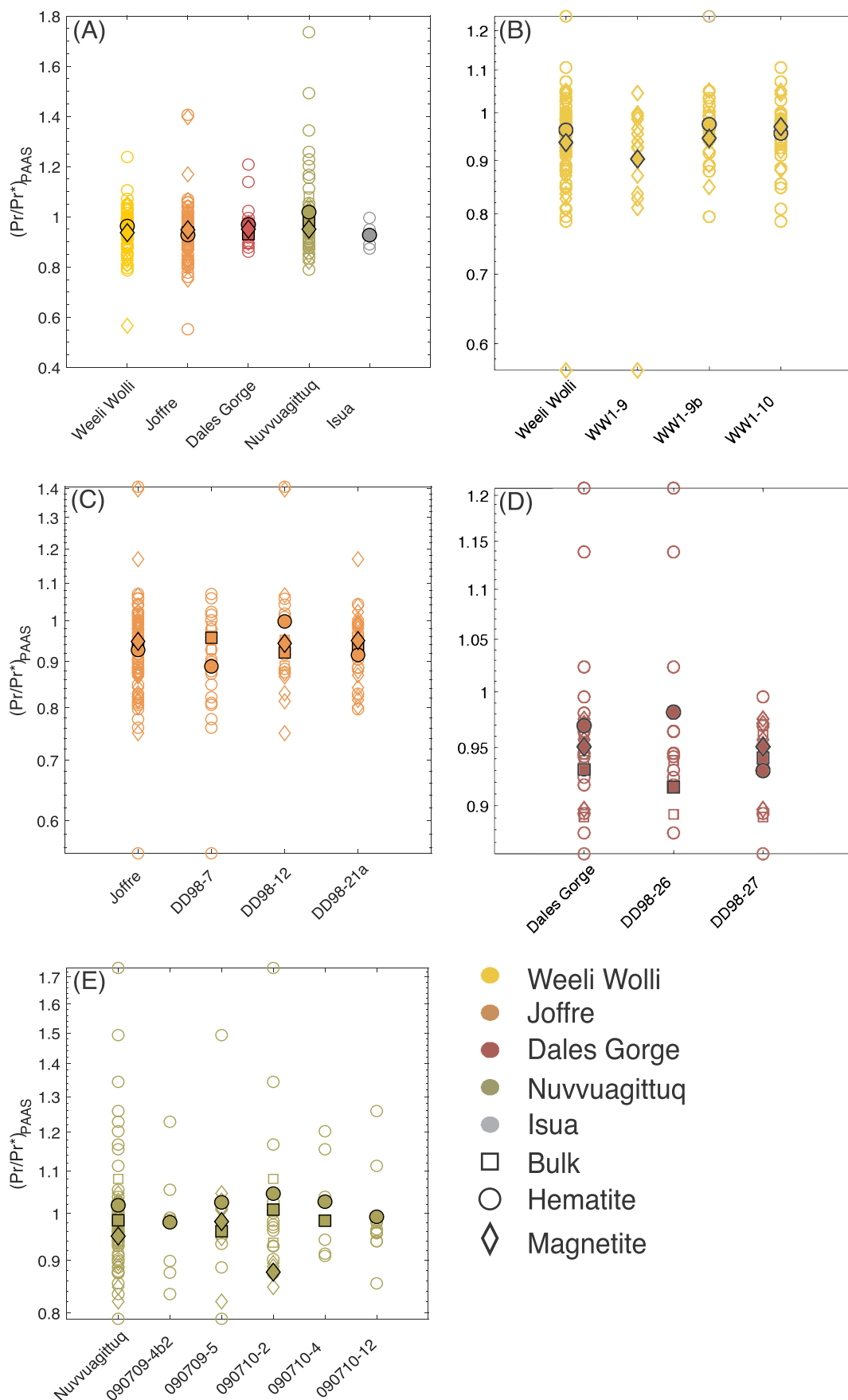
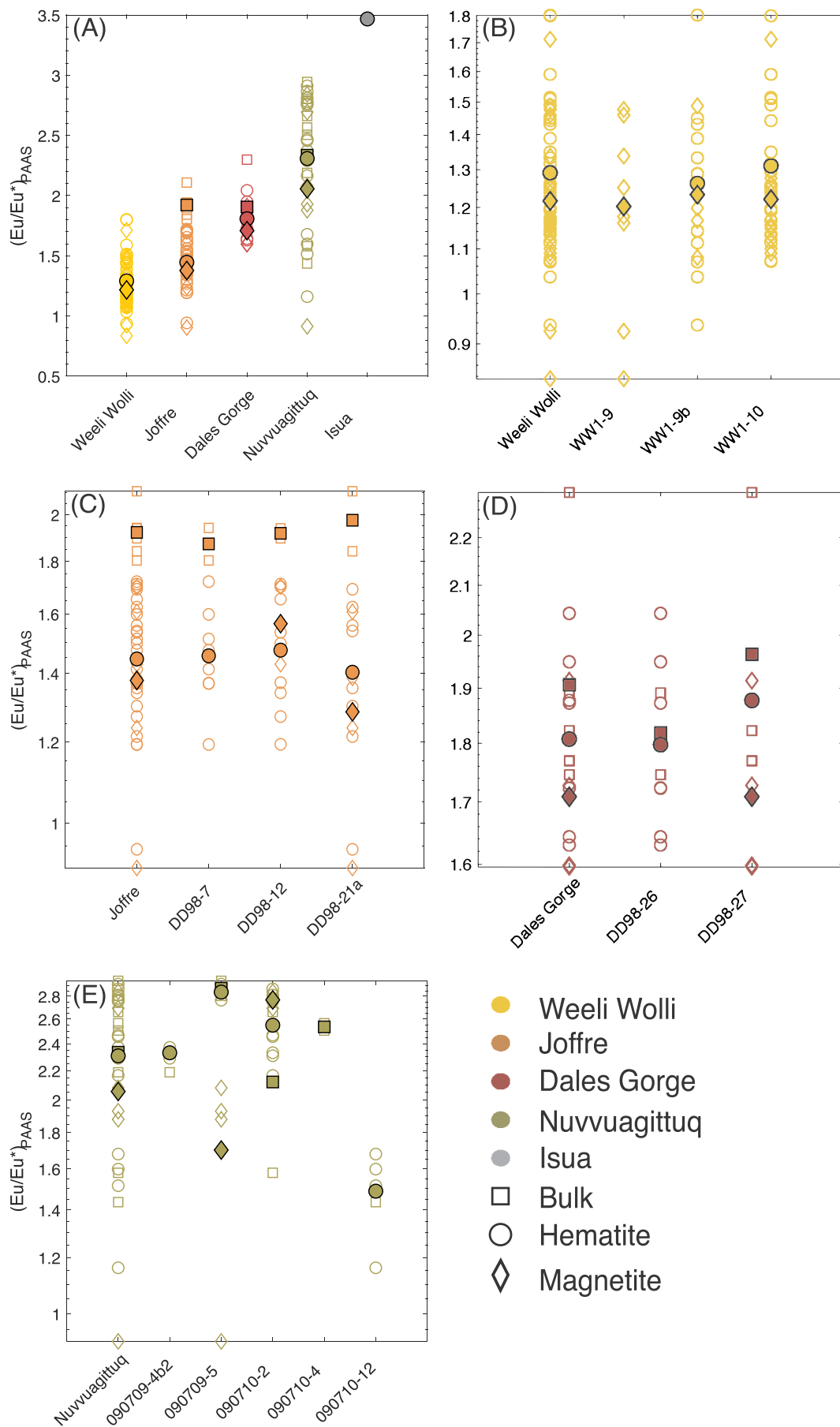
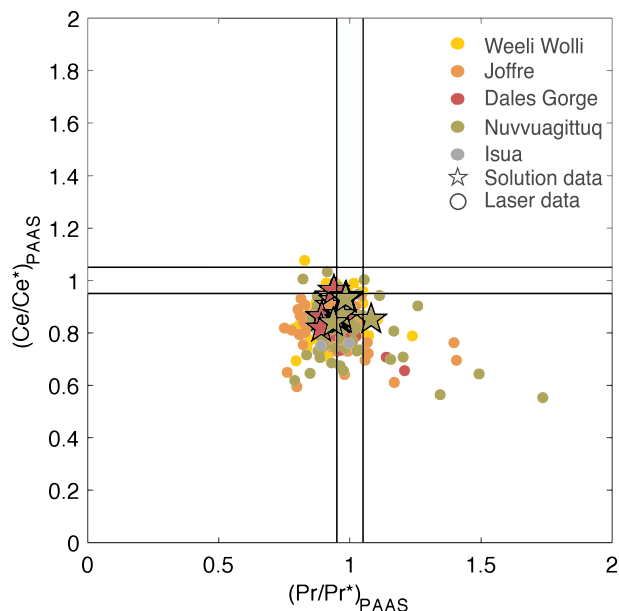


Fig. 14. Inter-deposit comparison for  $Ce/Ce^*_{PAAS}$  calculated after Bau and Dulski (1996) (A), and intra-deposit comparisons showing the cumulative formation data and that of constituent samples for the Weeli Wolli Iron Formation (B), Joffre Member (C) and Dales Gorge Member (D) of the Brockman Iron Formation, and the IFB of the Nuvvuagittuq Supracrustal Belt (E). PAAS normalization after Taylor and McLennan (1985).



(caption on next page)

**Fig. 15.** Inter-deposit comparison for  $\text{Eu}/\text{Eu}^*_{\text{PAAS}}$  calculated after Bau and Dulski (1996) (A), and intra-deposit comparisons showing the cumulative formation data and that of constituent samples for the Weeli Wolli Iron Formation (B), Joffre Member (C) and Dales Gorge Member (D) of the Brockman Iron Formation, and the BIF of the Nuvvuagittuq Supracrustal Belt (E). PAAS normalization after Taylor and McLennan (1985).



**Fig. 16.** Cross-plot of  $\text{Pr}/\text{Pr}^*$  versus  $\text{Ce}/\text{Ce}^*$  normalized to PAAS after Bau and Dulski (1996). True shale-normalized negative  $\text{Ce}/\text{Ce}^*$  fall in the lower right-hand quadrant of the diagram and are present for data generated by LA-HR-ICP-MS. Yet, bulk samples show no resolvable negative Ce anomalies, suggesting that bulk chemical digestions tend to dilute geochemical signals that are otherwise resolvable at the grain scale. Colors indicate their respective formations, consistent with previous figures. Stars indicate bulk digestions and circles laser generated data.

large compilations where the emphasis is on longer term, more dramatic first-order shifts in trace metal availability (e.g., Robbins et al., 2016).

While bulk digests likely offer a more conservative reflection of seawater composition, they may be ill-suited for capturing the true temporal variation in trace element enrichments within a given deposit, as some geochemical signals present at the mineral scale may be diluted or entirely cryptic. For instance, negative Ce anomalies are captured in laser ablation data from several formations, including the  $\geq 3.75$  Ga NSB, Joffre Member, and Weeli Wolli Iron Formation, while bulk rock data show muted or absent anomalies (Fig. 16). Negative Ce anomalies (as reflected by  $\text{Pr}/\text{Pr}^*_{\text{PAAS}} > 1$ ) are observed in laser data from the NSB BIF, (Fig. 16), and may be indicative of localized oxygen production at low levels during the deposition of NSB sediments. Alternatively, the negative Ce-anomaly observed in the NSB could be due to recent oxidative weathering of samples exposed at or close to the surface, or the partitioning of REE + Y during metamorphism of this unit. The potential for surface weathering to influence Ce anomalies has recently been demonstrated for the 2.95 Ga Ijzermijn iron formation, where small differences in Ce-anomalies are present between weathered outcrop and fresh drill core samples (Albut et al., 2018).

In order to resolve these possibilities, a detailed comparison between hand samples collected at the surface and fresh drill core is advised. Similarly, the exclusive consideration of bulk digestion data may dilute certain geochemical signals. The spike in BIF Cr concentrations identified by Konhauser et al. (2011) and attributed to the aerobic oxidation of pyrite on land and subsequent transport of Cr to BIF depositional basins is observable in bulk digest data, but even more pronounced in Cr records generated by LA-HR-ICP-MS (see their Fig. 1). Examples such as these suggest that when evaluating temporal records of BIF composition, an approach that utilizes a combination of laser and bulk digestion data is necessary to capture the range and variation of trace element concentrations within a given deposit and when comparing BIF through time.

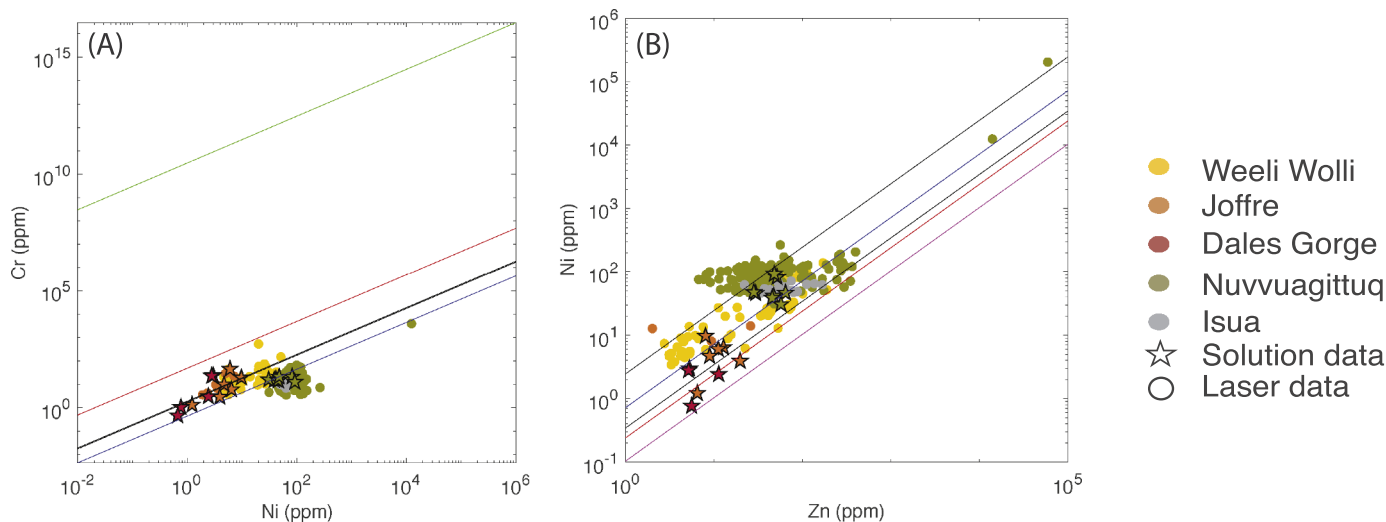


**Fig. 17.** Scaling of transition metals (A) Cr vs. Ni, (B) Cr vs. Mo, (C) Mo vs. Zn, and (D) Ni vs. Zn. All transition metals pairs examined here show relatively strong linear scaling. Overlain are expected scaling factors based on the ratios of transition metals in modern seawater (blue; Bruland et al., 2014), the first binding constants for strong sites on hydrous ferric oxides (red; Dzombak and Morel, 1990), the possible range of upper continental crust (black; Condie, 1993; Rudnick and Gao, 2014), and biomass of the marine photoferrotoph *Rhodovulum iodosum* (magenta; Konhauser et al., 2018). For (B), the green line represents the expected scaling for Cr and Zn given the binding constants for chromate and Zn, while the red line is trivalent Cr to Zn (Dzombak and Morel, 1990). Stars represent bulk solution data, while circles represent in-situ LA-HR-ICP-MS analyses. (For interpretation of the references to colour in this figure legend, the reader is referred to the web version of this article.)

**Table 2**  
Expected stoichiometric scaling for possible exit pathways for trace elements to banded iron formations.

Ratio	Detrital - low <sup>a</sup>	Detrital - high <sup>a</sup>	Photoferrotrophs <sup>b</sup>	Seawater <sup>c</sup>	Adsorption constants (K <sub>1</sub> /K <sub>1</sub> ) <sup>d</sup>
Ni/Zn	0.343	2.448	0.103	0.718	0.240
Cr/Ni	1.744	1.913	–	0.443	48.978
Chromate/Zn	–	–	–	–	7.24 × 10 <sup>9</sup>
Chromate/Ni	–	–	–	–	3.02 × 10 <sup>10</sup>

<sup>a</sup> Values represent the widest possible range from the combination of Condie (1993) and Rudnick and Gao (2014).

<sup>b</sup> Photoferrotroph values from Konhauser et al. (2018).

<sup>c</sup> Values from Bruland et al. (2014).

## 6. Conclusions

Although BIF are critical archives for understanding the trace element and redox evolution of seawater, the variance of trace element concentrations and trace element to iron ratios within a given deposit, and the comparability of laser ablation to bulk rock digestion data, has remained understudied. Intra-formational comparisons of bulk digestion versus LA-HR-ICP-MS data reveal that some of the variation observed within a given BIF deposit is derived from heterogeneity at the micro-scale, as one may well expect. Mean formation values for bulk versus laser ablation data, however, can differ significantly for a given BIF sample, but are typically within an order of magnitude of each other. This suggests an overall fidelity of the BIF record in capturing authigenic seawater signatures at a variety of scales, but also an inherent need to examine both bulk digestion and laser ablation data to capture the full range of information recorded in the elemental composition of BIF.

As variability is generally less for solution mode analyses of bulk samples, these samples likely provide more conservative estimates for ancient seawater but, as a result, may dilute or obscure geochemical signals that can be detected using a higher-resolution in situ technique such as LA-HR-ICP-MS. For instance, we found previously undocumented negative Ce anomalies in Archean to Paleoproterozoic BIF at the grain scale that are cryptic at the bulk-rock scale. These negative Ce anomalies, generally considered indicative of oxygen at the time of formation, have been identified in BIF samples from the ≥ 3.75 Ga NSB. Whether these are the result of an ancient oxygenic phototrophic metabolism or the result of more recent outcrop weathering remains a critical question for future research. The results presented here highlight the advantage of a combined approach utilizing both bulk and LA-HR-ICP-MS geochemical analyses of BIF to assess the trace element and redox evolution of ancient seawater.

While no single cause for the variability can be unambiguously identified, variation in trace element concentrations within a given formation are likely the combination of subtle shifts in environmental controls, vectors delivering the trace elements to the BIF depositional setting, and localized diagenetic to metamorphic effects within the sediment pile. Nonetheless, the BIF record captures first-order trends in trace element abundances consistent with other marine chemical sedimentary records (e.g., black shales, pyrites), supporting the assertion that these are archiving changes in Precambrian seawater composition.

Supplementary data to this article can be found online at <https://doi.org/10.1016/j.chemgeo.2018.12.036>.

## Acknowledgements

Bleuenn Guéguen is thanked for assistance with LA-HR-ICP-MS analyses performed at the European Institute for Marine Studies. This work was supported by a Mobility of Foreign PhD students in Brittany Grant from the Université de Bretagne Occidentale and a Vanier Canada Graduate Scholarship to Leslie Robbins, NSERC Discovery Grants to Kurt Konhauser (RGPIN-165831) and Daniel Alessi (RGPIN-04134), and LabexMER funding from the European Institute for Marine Studies

(LabexMER, ANR-10-LABX-19) to Stefan Lalonde. We thank Dr. Eva Stüeken and an anonymous reviewer for comments that helped to greatly improved this manuscript.

## References

- Ahn, J.H., Buseck, P.R., 1990. Hematite nanospheres of possible colloidal origin from a Precambrian banded iron formation. *Science* 250, 111–113.
- Albut, G., Babechuk, M.G., Kleinhans, I.C., Bengler, M., Beukes, N.J., Steinhilber, B., Smith, A.J.B., Kruger, S.J., Schoenberg, R., 2018. Modern rather than Mesoarchean oxidative weathering responsible for the heavy stable Cr isotopic signatures of the 2.95 Ga old Ijzermijn iron formation (South Africa). *Geochim. Cosmochim. Acta* 228, 157–189.
- Alibert, C., 2016. Rare earth elements in Hamersley BIF minerals. *Geochim. Cosmochim. Acta* 184, 311–328.
- Anbar, A.D., Knoll, A.H., 2002. Proterozoic ocean chemistry and evolution: a bioinorganic bridge? *Science* 297, 1137–1142.
- Baldwin, G.J., Thurston, P.C., Kamber, B.S., 2011. High-precision rare earth element, nickel, and chromium chemistry of chert microbands pre-screened with in-situ analysis. *Chem. Geol.* 285, 133–143.
- Barley, M.E., Pickard, A., Sylvester, P., 1997. Emplacement of a large igneous province as a possible cause of banded iron formation 2.45 billion years ago. *Nature* 385, 55–58.
- Bau, M., 1993. Effects of syn- and post-depositional processes on the rare-earth element distribution in Precambrian iron-formations. *Eur. J. Mineral.* 5, 257–267.
- Bau, M., Dulski, P., 1996. Distribution of yttrium and rare-earth elements in the Penge and Kuruman iron-formations, Transvaal Supergroup, South Africa. *Precambrian Res.* 79, 37–55.
- Bau, M., Möller, P., 1993. Rare earth element systematics of the chemically precipitated component in Early Precambrian iron formations and the evolution of the terrestrial atmosphere-hydrosphere-lithosphere system. *Geochim. Cosmochim. Acta* 57, 2239–2249.
- Bekker, A., Slack, J.F., Planavsky, N., Krapez, B., Hofmann, A., Konhauser, K.O., Rouxel, O.J., 2010. Iron formation: the sedimentary product of a complex interplay among mantle, tectonic, oceanic, and biospheric processes. *Econ. Geol.* 105, 467–508.
- Bekker, A., Planavsky, N., Krapez, B., Rasmussen, B., Hofmann, A., Slack, J., Rouxel, O.J., Konhauser, K.O., 2014. Iron formations: their origins and implications for ancient seawater chemistry. In: Holland, H.D., Turekian, K. (Eds.), *Treatise on Geochemistry, Second edition*. Elsevier Ltd., pp. 561–628 (Treatise on Geochemistry).
- Bjerrum, C.J., Canfield, D.E., 2002. Ocean productivity before about 1.9 Gyr ago limited by phosphorus adsorption onto iron oxides. *Nature* 417, 159–162.
- Bolhar, R., Kamber, B., Moorbath, S., Fedo, C., Whitehouse, M., 2004. Characterisation of early Archaean chemical sediments by trace element signatures. *Earth Planet. Sci. Lett.* 222, 43–60.
- Bruland, K.W., Middag, R., Lohan, M.C., Holland, H.D., Turekian, K., 2014. Controls of trace metals in seawater. In: *Treatise on Geochemistry, Second edition*. vol. 8. Elsevier Ltd., pp. 19–51.
- Cates, N.L., Mojzsis, S.J., 2007. Pre-3750 Ma supracrustal rocks from the Nuvvuagittuq supracrustal belt, northern Québec. *Earth Planet. Sci. Lett.* 255, 9–21.
- Cates, N.L., Mojzsis, S.J., 2009. Metamorphic zircon, trace elements and Neoproterozoic metamorphism in the ca. 3.75 Ga Nuvvuagittuq supracrustal belt, Québec (Canada). *Chem. Geol.* 261, 99–114.
- Chi Fru, E., Rodríguez, N.P., Partin, C.A., Lalonde, S.V., Andersson, P.S., Weiss, D.J., El Albani, A., Rodushkin, I., Konhauser, K.O., 2016. Cu isotopes in marine black shales record the Great Oxidation Event. *Proc. Natl. Acad. Sci. U. S. A.* 113, 4941–4946.
- Condie, K.C., 1993. Chemical composition and evolution of the upper continental crust: contrasting results from surface samples and shales. *Chem. Geol.* 104, 1–37.
- David, J., Godin, L., Stevenson, R., O'Neil, J., Francis, D., 2009. U-Pb ages (3.8–2.7 Ga) and Nd isotope data from the newly identified Eoarchean Nuvvuagittuq supracrustal belt, Superior Craton, Canada. *Geol. Soc. Am. Bull.* 121, 150–163.
- Davy, R., 1983. A contribution to the chemical composition of Precambrian iron-formations. In: Trendall, A.F., Morris, R.C. (Eds.), *Iron-formation Facts and Problems, Developments in Precambrian Geology*. Elsevier, pp. 325–343 (Chapter 8).
- Davy, R., 1992. Mineralogy and Chemical Composition of a Core From the Weeli Weeli Formation in the Hamersley Basin (No. Record 1991/6). Geological Survey of Western Australia, Perth, pp. 1–103.
- De Carlo, E.H., Green, W.J., 2002. Rare earth elements in the water column of Lake Vanda, McMurdo Dry Valleys, Antarctica. *Geochim. Cosmochim. Acta* 66,

- 1323–1333.
- Derry, L., Jacobsen, S., 1990. The chemical evolution of Precambrian seawater: evidence from REEs in banded iron formations. *Geochim. Cosmochim. Acta* 54, 2965–2977.
- Dodd, M.S., Papineau, D., Grenne, T., Slack, J.F., Rittner, M., Pirajno, F., O'Neil, J., Little, C.T.S., 2017. Evidence for early life in Earth's oldest hydrothermal vent precipitates. *Nature* 543, 60–64.
- Dupont, C.L., Butcher, A., Valas, R.E., Bourne, P.E., Caetano-Anollés, G., 2010. History of biological metal utilization inferred through phylogenomic analysis of protein structures. *Proc. Natl. Acad. Sci. U. S. A.* 107, 10567–10572.
- Dzombak, D.A., Morel, F.M.M., 1990. Surface complexation modeling. Wiley-Interscience 1–393.
- Eickmann, B., Hofmann, A., Wille, M., Bui, T.H., Wing, B.A., Schoenberg, R., 2018. Isotopic evidence for oxygenated Mesoarchean shallow oceans. *Nat. Geosci.* 11, 133–138.
- Frei, R., Crowe, S.A., Bau, M., Polat, A., Fowle, D.A., 2016. Oxidative elemental cycling under the low O<sub>2</sub> Eoarchean atmosphere. *Sci. Rep.* 6, 21058.
- Guillong, M., Meier, D.L., Allan, M.M., Heinrich, C.A., Yardley, B.W.D., 2008. SILLS: A MATLAB-based Program for the Reduction of Laser Ablation ICP-MS Data of Homogeneous Materials and Inclusions. Mineralogical Association of Canada Short Course 40, Vancouver, B.C., pp. 328–333.
- Halama, M., Swanner, E.D., Konhauser, K.O., Kappler, A., 2016. Evaluation of siderite and magnetite formation in BIFs by pressure–temperature experiments of Fe(III) minerals and microbial biomass. *Earth Planet. Sci. Lett.* 450, 243–253.
- Haugaard, R., Pecoits, E., Lalonde, S.V., Rouxel, O.J., Konhauser, K.O., 2016. The Joffre banded iron formation, Hamersley Group, Western Australia: assessing the palaeoenvironment through detailed petrology and geostratigraphy. *Precambrian Res.* 273, 12–37.
- Holland, H., 1973. The oceans: a possible source of iron in iron-formations. *Econ. Geol.* 68, 1169–1172.
- Holland, H.D., 1978. *The Chemistry of the Atmosphere and Oceans*. Wiley, New York, pp. 1–369.
- Hsu, J.C., 1996. *Multiple Comparisons. Theory and Methods*. Chapman and Hall, London, England.
- Isley, A., 1995. Hydrothermal plumes and the delivery of iron to banded iron formation. *The J. Geol.* 169–185.
- Jochum, K.P., Nohl, U., Herwig, K., Lammel, E., Stoll, B., Hofmann, A.W., 2005. GeoReM: a new geochemical database for reference materials and isotopic standards. *Geostand. Geoanal. Res.* 29, 333–338. <https://doi.org/10.1111/j.1751-908x.2005.tb00904.x>. (Accessed December 3, 2018).
- Johnson, C.M., Beard, B.L., Klein, C., Beukes, N., Roden, E., 2008. Iron isotopes constrain biologic and abiologic processes in banded iron formation genesis. *Geochim. Cosmochim. Acta* 72, 151–169.
- Klein, C., 2005. Some Precambrian banded iron-formations (BIFs) from around the world: their age, geologic setting, mineralogy, metamorphism, geochemistry, and origins. *Am. Mineral.* 90, 1473–1499.
- Köhler, I., Konhauser, K.O., Papineau, D., Bekker, A., Kappler, A., 2013. Biological carbon precursor to diagenetic siderite with spherical structures in iron formations. *Nat. Commun.* 4, 1741.
- Konhauser, K.O., Hamade, T., Raiswell, R., Morris, R., Ferris, F., Southam, G., Canfield, D., 2002. Could bacteria have formed the Precambrian banded iron formations? *Geology* 30, 1079–1082.
- Konhauser, K.O., Newman, D., Kappler, A., 2005. The potential significance of microbial Fe (III) reduction during deposition of Precambrian banded iron formations. *Geobiology* 3, 167–177.
- Konhauser, K.O., Lalonde, S.V., Amskold, L.A., Holland, H., 2007. Was there really an Archean phosphate crisis? *Science* 315, 1234.
- Konhauser, K.O., Pecoits, E., Lalonde, S.V., Papineau, D., Nisbet, E.G., Barley, M.E., Arndt, N.T., Zahnle, K., Kamber, B.S., 2009. Oceanic nickel depletion and a methanogen famine before the Great Oxidation Event. *Nature* 458, 750–753.
- Konhauser, K.O., Lalonde, S.V., Planavsky, N.J., Pecoits, E., Lyons, T.W., Mojzsis, S.J., Rouxel, O.J., Barley, M.E., Rosière, C.A., Fralick, P.W., Kump, L.R., Bekker, A., 2011. Aerobic bacterial pyrite oxidation and acid rock drainage during the Great Oxidation Event. *Nature* 478, 369–373.
- Konhauser, K.O., Robbins, L.J., Pecoits, E., Peacock, C., Kappler, A., Lalonde, S.V., 2015. The Archean nickel famine revisited. *Astrobiology* 15, 804–815.
- Konhauser, K.O., Planavsky, N.J., Hardisty, D.S., Robbins, L.J., Warchola, T.J., Haugaard, R., Lalonde, S.V., Partin, C.A., Oonk, P.B.H., Tsikos, H., Lyons, T.W., Bekker, A., Johnson, C.M., 2017. Iron formations: a global record of Neoproterozoic to Palaeoproterozoic environmental history. *Earth-Sci. Rev.* 172, 140–177.
- Konhauser, K.O., Robbins, L.J., Alessi, D.S., Flynn, S.L., Gingras, M.K., Martinez, R.E., Kappler, A., Swanner, E.D., Li, Y.-L., Crowe, S.A., Planavsky, N.J., Reinhard, C.T., Lalonde, S.V., 2018. Phytoplankton contributions to the trace-element composition of Precambrian banded iron formations. *Geol. Soc. Am. Bull.* 130, 941–951.
- Krapež, B., Barley, M.E., Pickard, A.L., 2003. Hydrothermal and resedimented origins of the precursor sediments to banded iron formation: sedimentological evidence from the Early Palaeoproterozoic Brockman Supersequence of Western Australia. *Sedimentology* 50, 979–1011.
- Lalonde, S.V., Smith, D., Owttrim, G., Konhauser, K.O., 2008. Acid-base properties of cyanobacterial surfaces. II: silica as a chemical stressor influencing cell surface reactivity. *Geochim. Cosmochim. Acta* 72, 1269–1280.
- Li, Y.L., Konhauser, K.O., Cole, D.R., Phelps, T.J., 2011. Mineral ecophysiological data provide growing evidence for microbial activity in banded-iron formations. *Geology* 39, 707–710.
- Lyons, T.W., Reinhard, C.T., Planavsky, N.J., 2014. The rise of oxygen in Earth's early ocean and atmosphere. *Nature* 506, 307–315.
- Magnabosco, C., Moore, K.R., Wolfe, J.M., Fournier, G.P., 2018. Dating phototropic microbial lineages with reticulate gene histories. *Geobiology* 16, 179–189.
- Martinez, R.E., Konhauser, K.O., Paunova, N., Wu, W., Alessi, D.S., Kappler, A., 2016. Surface reactivity of the anaerobic phototrophic Fe (II)-oxidizing bacterium *Rhodovulum iodosum*: implications for trace metal budgets in ancient oceans and banded iron formations. *Chem. Geol.* 442, 113–120.
- McLennan, S., 1989. Rare earth elements in sedimentary rocks: influence of provenance and sedimentary processes. In: Lipin, B.R., McKay, G.A. (Eds.), *Geochemistry and Mineralogy of Rare Earth Elements*. *Rev. Mineral. Geochem.* vol. 21, pp. 169–200.
- Miyano, T., Klein, C., 1984. Evaluation of the stability relations of amphibole asbestos in metamorphosed iron formations. *Min. Geol.* 33, 213–222.
- Mloszewska, A., Pecoits, E., Cates, N., Mojzsis, S.J., O'Neil, J., Robbins, L.J., Konhauser, K.O., 2012. The composition of Earth's oldest iron formations: the Nuvvuagittuq Supracrustal Belt (Québec, Canada). *Earth Planet. Sci. Lett.* 317–318, 331–342.
- Mloszewska, A.M., Mojzsis, S.J., Pecoits, E., Papineau, D., Dauphas, N., Konhauser, K.O., 2013. Chemical sedimentary protoliths in the > 3.75 Ga Nuvvuagittuq Supracrustal Belt (Québec, Canada). *Gondwana Res.* 23, 574–594.
- Morris, R., 1993. Genetic modelling for banded iron-formation of the Hamersley Group, Pilbara Craton, Western Australia. *Precambrian Res.* 60, 243–286.
- O'Neil, J., Carlson, R.W., 2017. Building Archean cratons from Hadean mafic crust. *Science* 355, 1199–1202.
- O'Neil, J., Maurice, C., Stevenson, R.K., Larocque, J., Cloquet, C., David, J., Francis, D., 2007. The geology of the 3.8 Ga Nuvvuagittuq (Porpoise Cove) greenstone belt, northeastern Superior Province, Canada. *Dev. Precambrian Geol.* 15, 219–250.
- O'Neil, J., Carlson, R., Francis, D., Stevenson, R., 2008. Neodymium-142 evidence for Hadean mafic crust. *Science* 321, 1828–1831.
- O'Neil, J., Francis, D., Carlson, R.W., 2011. Implications of the Nuvvuagittuq greenstone belt for the formation of Earth's early crust. *J. Phys. Chem.* 52, 985–1009.
- Oonk, P.B.H., Tsikos, H., Mason, P.R.D., Henkel, S., Staubwasser, M., Fryer, L., Poulton, S.W., Williams, H.M., 2017. Fraction-specific controls on the trace element distribution in iron formations — implications for trace metal stable isotope proxies. *Chem. Geol.* 474, 17–32.
- Oonk, P.B.H., Mason, P.R.D., Tsikos, H., Bau, M., 2018. Fraction-specific rare earth elements enable the reconstruction of primary seawater signatures from iron formations. *Geochim. Cosmochim. Acta* 238, 102–122.
- Partin, C.A., Lalonde, S.V., Planavsky, N.J., Bekker, A., Rouxel, O.J., Lyons, T.W., Konhauser, K.O., 2013a. Uranium in iron formations and the rise of atmospheric oxygen. *Chem. Geol.* 362, 82–90.
- Partin, C.A., Bekker, A., Planavsky, N.J., Scott, C.T., Gill, B.C., Li, C., Podkovyrov, V., Maslov, A., Konhauser, K.O., Lalonde, S.V., Love, G.D., Poulton, S.W., Lyons, T.W., 2013b. Large-scale fluctuations in Precambrian atmospheric and oceanic oxygen levels from the record of U in shales. *Earth Planet. Sci. Lett.* 369–370, 284–293.
- Pecoits, E., Gingras, M.K., Barley, M.E., Kappler, A., Posth, N.R., Konhauser, K.O., 2009. Petrography and geochemistry of the Dales Gorge banded iron formation: paragenetic sequence, source and implications for palaeo-ocean chemistry. *Precambrian Res.* 172, 163–187.
- Pickard, A., 2002. SHRIMP U–Pb zircon ages of tuffaceous mudrocks in the Brockman Iron Formation of the Hamersley Range, Western Australia. *Aust. J. Earth Sci.* 49, 491–507.
- Planavsky, N.J., Rouxel, O.J., Bekker, A., Lalonde, S.V., Konhauser, K.O., Reinhard, C.T., Lyons, T.W., 2010a. The evolution of the marine phosphate reservoir. *Nature* 467, 1088–1090.
- Planavsky, N., Bekker, A., Rouxel, O.J., Kamber, B., Hofmann, A., Knudsen, A., Lyons, T.W., 2010b. Rare earth element and yttrium compositions of Archean and Paleoproterozoic Fe formations revisited: new perspectives on the significance and mechanisms of deposition. *Geochim. Cosmochim. Acta* 74, 6387–6405.
- Planavsky, N.J., Asael, D., Hofmann, A., Reinhard, C.T., Lalonde, S.V., Knudsen, A., Wang, X., Ossa Ossa, F., Pecoits, E., Smith, A.J.B., Beukes, N.J., Bekker, A., Johnson, T.M., Konhauser, K.O., Lyons, T.W., Rouxel, O.J., 2014. Evidence for oxygenic photosynthesis half a billion years before the Great Oxidation Event. *Nat. Geosci.* 7, 283–286.
- Posth, N.R., Köhler, I., Swanner, E.D., Schröder, C., Wellmann, E., Binder, B., Konhauser, K.O., Neumann, U., Berthold, C., Nowak, M., Kappler, A., 2013. Simulating Precambrian banded iron formation diagenesis. *Chem. Geol.* 362, 66–73.
- Robbins, L.J., Lalonde, S.V., Saito, M.A., Planavsky, N.J., Mloszewska, A.M., Pecoits, E., Scott, C., Dupont, C.L., Kappler, A., Konhauser, K.O., 2013. Authigenic iron oxide proxies for marine zinc over geological time and implications for eukaryotic metallome evolution. *Geobiology* 11, 295–306.
- Robbins, L.J., Swanner, E.D., Lalonde, S.V., Eickhoff, M., Paranich, M.L., Reinhard, C.T., Peacock, C.L., Kappler, A., Konhauser, K.O., 2015. Limited Zn and Ni mobility during simulated iron formation diagenesis. *Chem. Geol.* 402, 30–39.
- Robbins, L.J., Lalonde, S.V., Planavsky, N.J., Partin, C.A., Reinhard, C.T., Kendall, B., Scott, C., Hardisty, D.S., Gill, B.C., Alessi, D.S., Dupont, C.L., Saito, M.A., Crowe, S.A., Poulton, S.W., Bekker, A., Lyons, T.W., Konhauser, K.O., 2016. Trace elements at the intersection of marine biological and geochemical evolution. *Earth-Sci. Rev.* 163, 323–348.
- Rudnick, R.L., Gao, S., 2014. Composition of the continental crust. In: Holland, H.D., Turekian, K. (Eds.), *Treatise on Geochemistry*, Second edition. vol. 4. Elsevier Ltd., pp. 1–51.
- Sahoo, S.K., Planavsky, N.J., Kendall, B., Wang, X., Shi, X., Scott, C., Anbar, A.D., Lyons, T.W., Jiang, G., 2012. Ocean oxygenation in the wake of the Marinoan glaciation. *Nature* 488, 546–549.
- Satkoski, A.M., Beukes, N.J., Li, W., Beard, B.L., Johnson, C.M., 2015. A redox-stratified ocean 3.2 billion years ago. *Earth Planet. Sci. Lett.* 430, 43–53.
- Scott, C., Lyons, T.W., Bekker, A., Shen, Y., Poulton, S.W., Chu, X., Anbar, A.D., 2008. Tracing the stepwise oxygenation of the Proterozoic ocean. *Nature* 452, 456–459.
- Scott, C., Planavsky, N.J., Dupont, C.L., Kendall, B., Gill, B.C., Robbins, L.J., Husband,

- K.F., Arnold, G.L., Wing, B.A., Poulton, S.W., Bekker, A., Anbar, A.D., Konhauser, K.O., Lyons, T.W., 2013. Bioavailability of zinc in marine systems through time. *Nat. Geosci.* 6, 125–128.
- Shih, P.M., Hemp, J., Ward, L.M., Matzke, N.J., Fischer, W.W., 2016. Crown group Oxyphotobacteria postdate the rise of oxygen. *Geobiology* 15, 19–29.
- Smith, R.E., Perdrix, J.L., Parks, T.C., 1982. Burial metamorphism in the Hamersley Basin, Western Australia. *J. Petrol.* 23, 75–102.
- Sun, S., Konhauser, K.O., Kappler, A., Li, Y.-L., 2015. Primary hematite in Neoproterozoic to Paleoproterozoic oceans. *Geol. Soc. Am. Bull.* 127, 850–861.
- Swanner, E.D., Planavsky, N.J., Lalonde, S.V., Robbins, L.J., Bekker, A., Rouxel, O.J., Saito, M.A., Kappler, A., Mojzsis, S.J., Konhauser, K.O., 2014. Cobalt and marine redox evolution. *Earth Planet. Sci. Lett.* 390, 253–263.
- Taylor, S.R., McLennan, S.M., 1985. *The Continental Crust: Its Composition and Evolution - An Examination of the Geochemical Record Preserved in Sedimentary Rocks*. Blackwell Scientific Publications, Oxford, pp. 1–312.
- Trendall, A.F., Blockley, J.G., 1970. The iron formations of the Precambrian Hamersley Group Western Australia with special reference to the associated crocidolite. *Geol. Surv. W. Aust. Bull.* 119, 1–366.
- Trendall, A., Compston, W., De Laeter, D., Bennett, V., 2004. SHRIMP zircon ages constraining the depositional chronology of the Hamersley Group, Western Australia\*. *Aust. J. Earth Sci.* 51, 621–644.
- Viehmann, S., Bau, M., Hoffmann, J.E., Münker, C., 2015. Geochemistry of the Krivoy Rog Banded Iron Formation, Ukraine, and the impact of peak episodes of increased global magmatic activity on the trace element composition of Precambrian seawater. *Precambrian Res.* 270, 165–180.
- Warchola, T., Lalonde, S.V., Pecoits, E., Robbins, L.J., Alessi, D.S., Philippot, P., Konhauser, K.O., 2018. Petrological and geochemical analyses of the Boolgeeda Iron Formation, Hamersley Basin, Western Australia. *Precambrian Res.* 316, 155–173.
- Ward, L.M., Kirschvink, J.L., Fischer, W.W., 2016. Timescales of oxygenation following the evolution of oxygenic photosynthesis. *Orig. Life Evol. Biosph.* 46, 51–65.